A Novel Elasto-Geometric Model Exploiting Loaded Circular Test on a Machine Tool

Babak Beglarzadeh (✉ babak.beglarzadeh@polymtl.ca)

Polytechnique Montreal

René Mayer

Andreas Archenti

Research Article

A Novel Elasto-Geometric Model Exploiting Loaded Circular Test on a Machine Tool

Babak Beglarzadeh [a]*, René Mayer [a], Andreas Archenti [b]

[a] Department of Mechanical Engineering, Polytechnique Montreal, Montreal, QC, H3T 1J4, Canada

[b] Department of Production Engineering, KTH Royal Institute of Technology, Brinellvägen 68, Stockholm SE-10044, Sweden

* Corresponding author:

E-mail address: babak.beglarzadeh@polymtl.ca (Babak Beglarzadeh)

Abstract

A novel elasto-geometric model is introduced that simultaneously estimates joint compliances and geometric error parameters by employing the loaded double ball bar apparatus. The model parameters are estimated from tests at different force levels by distinguishing between errors that change with the applied force (compliance effect) from those that do not (geometric effects). At lower forces, the geometric errors are dominant whilst at higher forces compliance-induced errors dominate. By feeding the elasto-geometric model with pairs of adjacent force data the evolution of the estimated equivalent local compliance parameters and geometric errors with changes in the applied force are observed. Although theoretically unexpected, the estimated geometric errors also change across the force range. As the force increases the majority of equivalent compliance terms increase such as the dominant equivalent compliances C_{XXX} and C_{YYY} as well as the less significant compliances C_{XYX} and C_{CCY}. As for C_{CXY} and C_{CYY}, no clear trend was observed. Given this observed dependence of the compliance on the force level, the model was enriched by modeling the compliances as linear functions of the applied force. A single set of geometric errors could then be estimated and deemed valid across the load range. The root mean square error (RMSE) value for predicting the radial readings for all force levels for the constant and linearly variable compliance models are 0.0011 and 0.0009 mm, respectively, representing an 18% improvement for the linear compliance model. Both the constant and linearly variable compliance models exhibit over 91% fit to the experimental data with just over 1% improvement for the linear compliance model.

Keywords: Elasto-geometric model, joint compliance, geometric error, machine tool, numerical simulation

1. Introduction

Compliance in a machine tool results in changes in the location of its tool with respect to the workpiece in the presence of cutting forces and inertial and gravitational loads.

The tooltip stiffness chain was examined experimentally and with both analytical and finite element models [1]. The cutting force and the tool deflection were measured with a dynamometer and inductive proximity sensors, respectively. The tool deflection was found to contribute as much as the rest of the system. Tests were conducted one direction at a time with a single axis being moved very slowly to gradually increase the deflection. Results showed that the stiffness of shorter and thicker tools, and that of slender and flexible tools, were about 5 to 7 times and 15 times less than that of the machine and tool holder system, respectively.

The equivalent stiffness method models the joint deviation contribution to the total volumetric deviation under load [2] from measurements of the force versus deviation functions at the interface between the tool and workpiece. The translational compliances at the joints are modeled by a number of suitably oriented linear springs.

A static stiffness modeling of the machining space is introduced in [3]. The parametric model includes the six-directional static stiffness obtained by the combination of both load and deformation transfer matrices. The loading and deformation of each part of the machine are analyzed separately. To identify the static stiffness, an experimental setup is used including a loading device (hydraulic cylinder) to apply force in the X-, Y- and Z-direction and a displacement sensor to measure the deflection in the same direction. The error between the introduced model and measured stiffness was 7.6%.

The total stiffness of the machine is modeled using simple springs located at the bearing supports between the carriages and guideways [4]. Multi-body system theory is used to explain the topological structure of the machine. The deflection model represents the connection between the deformation of the components and the relative deformation of the tool and workpiece. To determine the stiffness value, each component was modeled as a spring with different degrees of freedom to deliver the resultant displacement in the direction of the force. The experimental data is gathered by applying a force to the machine spindle in either the X-, Y- or Z-direction and measuring the resulting deflection using an Eddy current proximity sensor. The difference between the estimated and given stiffness values at the tooltip was 8.8%, 9.6%, and 8.4% in the X-, Y- and Z-direction respectively.

To analyze the structural characteristics of an ultra-precision four-axis machine, the joint stiffness of both hydrostatic guideways of linear axes and hydrostatic bearings of the rotary C-axis were studied using a virtual prototype and experimental data [5]. The compliance of the individual axes and the stiffness of the overall machine loop were experimentally determined using a load cell and displacements measured by a laser interferometer. The virtual prototype was modeled in ANSYS software using solid elements as well as identifiable stiffness matrices for the four joints, which were identified to match the experimental joint compliances. The designed, predicted, and measured stiffness of the X- and Y-axis were 5.71, 4.68, and 4.98 (N/μm), and 9.86, 12.70, and 13.24 (N/μm), respectively. The predicted loop stiffness of the virtual prototype machine in the X-, Y- and Z-axis directions were 94%, 96%, and 93% of those experimentally measured.

In [6] the direction dependency of the tool to workpiece compliance of a machine tool was examined. A piezoelectric actuator excites the tool while the force and displacement are measured by a three-axis force sensor and three-axis accelerometer signals, respectively. The compliance in the X and Y (horizontal) directions was larger than that in the Z (vertical) direction. The highest compliance value in the X direction was two times larger than those in the Y and Z directions.

A device named Stiffness Workspace System (SWS) was introduced in [7]. It applies a force with a controlled value and direction and measures the resultant translational and rotational displacement using twelve inductive sensors. The machine is stationary. It was concluded that the stiffness varies both with the applied force direction and the location in the workspace.

An elastically Linked system (ELS) was introduced and the physical implementation was designed as a Loaded Double Ball Bar (LDBB) [8]. The LDBB measures the radial volumetric displacement during a circular test trajectory [9] while applying a constant radial force between the balls at the tool holder and workpiece table. The measurements provide the volumetric compliance i.e., the compliance in the working volume. It allows to test the machine in motion and combine the movement of two mechanical axes at various feed rates thus approaching more realistic conditions of use. A low force test is used as a reference and those readings are subtracted from data at higher force levels to remove contamination from no-load effects. Using data from an LDBB test, the accuracy of a machined part was predicted from the analysis of machining system capability [10]. In this approach, the volumetric deviations measured by an LDBB circular test are used to estimate a multi-body compliance model that can predict compliance for an arbitrary tool path. An FE model determines

the tool and workpiece contributions to the total deviation. This method predicted the machined workpiece geometry with about 17% error.

The unloaded telescopic ball bar was invented to measure the two- or three-dimensional accuracy of machine tools, as a fast and accurate method [11]. In [12] the characteristic patterns of ball bar traces for 2D circular tests in the XY, YZ, and XZ planes of a three linear axis machine tool due to a variety of machine error sources such as out-of-squareness and out-of-straightness were presented.

An elasto-geometrical calibration method for geometric errors and compliance parameters of a six-DOF serial robot was introduced [13]. The load was applied using weights at the end effector and the effect on the positioning was measured using a laser tracker. The torsional compliances, self-gravity, and weight center of gravity were estimated. The geometric errors included joint-dependent and joint-independent errors such as link offset and link twist errors.

An elasto-geometrical model of an industrial robot manipulator was introduced as a closed-loop mechanism [14]. The error model for geometrical calibration was developed to relate the positioning error to the vector of geometrical error through the Jacobian matrix. In the stiffness model, all the links of the closed-loop system were considered as beams and nodes. Six DOF for nodal displacement and wrench were considered. Elastic displacements were obtained through the stiffness model validated by the FEA model in CASTEM® software. It was shown that the link deformation was 20% of the total elastic displacement at the end effector.

To enhance robot manipulator static pose accuracy, an elasto-geometrical calibration was established [15]. Two methods were shown including analytical parametric modeling and a Takagi–Sugeno fuzzy inference system. In the first method, an analytical finite element theory was used to determine the equivalent stiffness of the structure that was required to predict the tool center point (TCP) pose error under a high load level. The geometrical and stiffness error parameters of the elasto-geometric model were identified. It was shown that by considering the whole working volume, measured elastic displacement depicted non-linear behavior that could not be explained by this method. Hence, a second method fuzzy interface, which had an efficient mathematical structure, was used to better explain the system's non-linear behavior. It was illustrated that by using this method, the accuracy of the TCP's pose had been improved down to $\pm$ 0.15mm.

An elasto-geometrical calibration approach was presented to improve the positioning accuracy of the industrial robot [16, 17]. A laser tracker was used to identify geometric parameter error and joint stiffness parameters by measuring the position of the end-effector in various robot configurations

while applying external forces and torques to the end effector with a cable-driven robot. The calibrated elasto-geometrical reduced the position error to 0.960 mm compared to 2.571 for a geometric-only calibration.

A model for machine tool equivalent joint compliance is introduced in [18]. Indirect estimation of joint compliance is carried out via the loaded circular test. The relationship between joint and volumetric compliance is established. It is shown that on-axis compliances such as C_{XXX} and C_{YYY} were dominant and their values slightly increased with the applied force. In this model, the effect of geometric errors was removed by subtracting the lowest force data assuming it only contained the effect of geometric errors.

In previously mentioned methods and models for machine tool stiffness, the effect of geometric error has not been considered. Furthermore, there is no analytical model to separate machine joint compliance and geometric error parameters' effect in the loaded status.

In the abovementioned robot elasto-geometric models and procedures, the kinematic model of the robot is used for the geometric errors model. It was also concluded that while the robot is under load, the kinematic calibration methods in which geometric factors were applied to identify model parameters, could not represent a significant improvement in the robot positioning accuracy since it is strongly affected by a high external load.

It is to be noted that the stiffness value can vary with the magnitude of the applied forces [18] which can be considered as a variable stiffness whilst it is not considered in the aforementioned methods and models. Nevertheless, the variable compliance model which analyzes the change of compliance parameters as a function of force is studied in this research.

In this research, the geometric errors and joint compliances are simultaneously estimated from two linear axis loaded double ball bar circular tests using an enriched elasto-geometric model whereby compliance is further modeled as a linear function of load to improve the separation of the contribution of compliance and geometric errors.

2. Machine geometric and compliance model

A geometrically perfect, thermally insensitive, and rigid machine tool locates its tool and workpiece to the desired relative location. However, manufacturing and assembly errors, wear and tear, collisions, thermal expansion, and the presence of forces and compliance are a few factors that cause the tool to deviate in location relative to the workpiece. A machine tool kinematics can be modeled

using a series of links and joints [19]. Machine deviations can be quantified as small errors in translations and rotations occurring at the attachment of each link between axis joints as axis alignment errors (or inter-axis errors) and each joint frame as error motion (intra-axis errors). These errors then propagate through the branches to the workpiece and tool. The difference between the actual and the nominal positions of the tool relative to the workpiece defines the volumetric error. A schematic of the kinematic model of the tested machine is illustrated in Fig. 1. As shown in Fig. 1 the LDBB circular test only involves the X- and Y-axis and since both are in the tool branch, the kinematic model of the deviated position of the tool with respect to the foundation frame can be written as

$${}^{\{F\},F}_{t'}P = {}^{F}_{Y_0}T\ {}^{Y_0}_{Y'_0}T\ {}^{Y'_0}_{Y}T\ {}^{Y}_{Y'}T\ {}^{Y'}_{X_0}T\ {}^{X_0}_{X'_0}T\ {}^{X'_0}_{X}T\ {}^{X}_{X'}T\ {}^{X'}_{t}T\ {}^{t}_{t'}T\ [0\quad 0\quad 0\quad 1]^{T} \qquad \text{Equation 1}$$

in which ${}^{i}_{j}T$ is the homogeneous transformation matrix (HTM) from frame i to frame j. ${}^{F}_{Y_0}T$ is the nominal location of the Y-axis and it is identity as the foundation frame and the Y-axis carriage frame at y=0 cannot be distinguished from each other, since the Y-axis is the primary reference then ${}^{Y_0}_{Y'_0}T$ is also identity, ${}^{Y'_0}_{Y}T$ is the nominal motion of the Y-axis, ${}^{Y}_{Y'}T$ is error motion of the Y-axis, ${}^{Y'}_{X_0}T$ is identity as the X-axis is nominally aligned with the *i*-axis of frame Y' and the X-axis location error, here an out-of-squareness error, will be modeled as a linear straightness error, then ${}^{X_0}_{X'_0}T$ is identity, ${}^{X'_0}_{X}T$ is the nominal motion of the X-axis, ${}^{X}_{X'}T$ is the error motion of the X-axis and ${}^{X'}_{t}T$ is identity as the nominal tool ball is assumed to be nominally at the moving carriage frame origin. ${}^{t}_{t'}T$ is the setup error on the tool ball. The LDBB test is conducted within a single XY plane and since the LDBB test
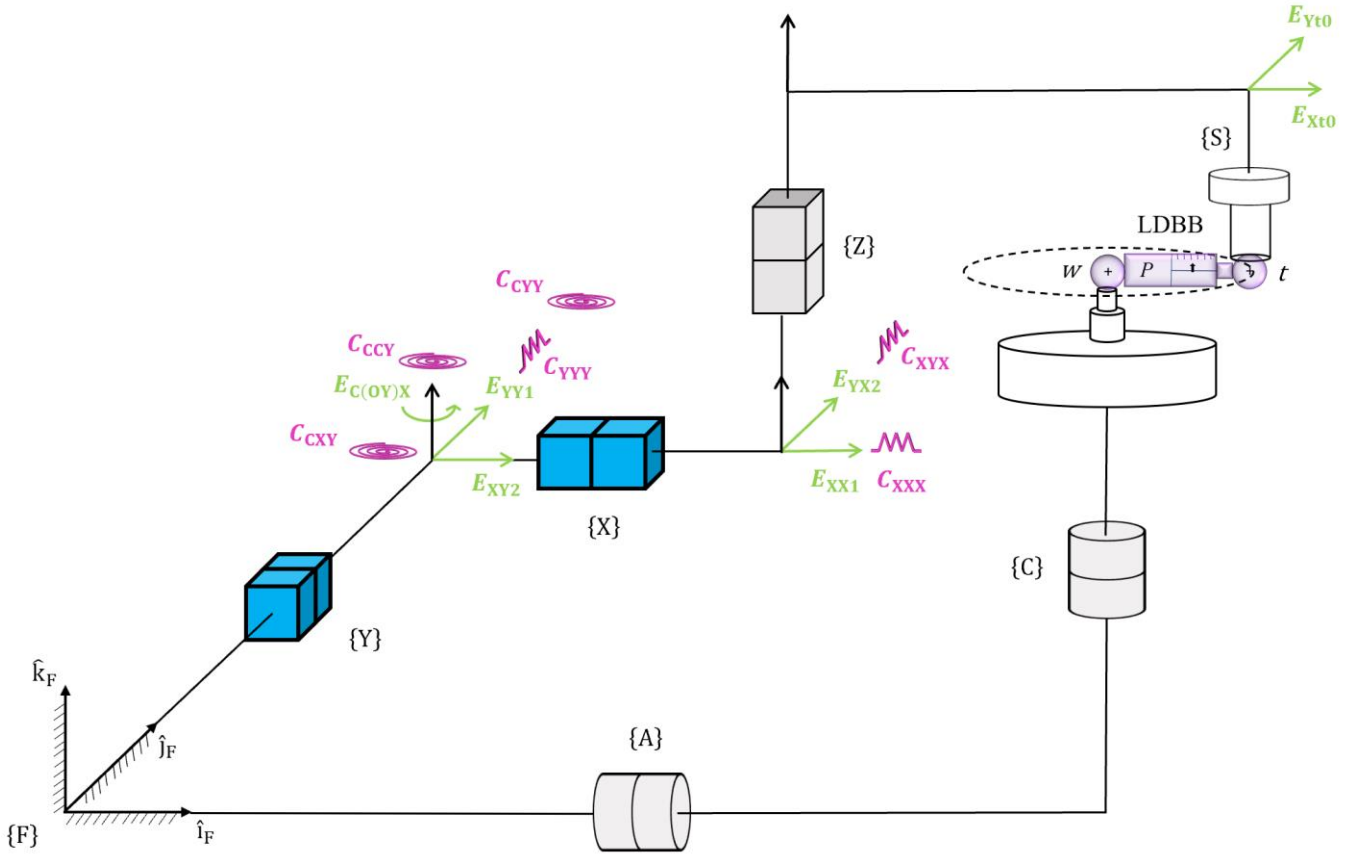
Fig. 1. Schematic of the nominal model for the LDBB test and its circular path through the XY plane along with the machine with the topology of wCAFYXZSt where S stands for the spindle axis. Only the X- and Y-axis, shown in blue, are active during the LDBB circular test. Compliance and geometric parameters are shown in magenta and green color, respectively.

does not provide readings out of the XY plane, only the error terms that can affect the ball bar readings are retained. The matrices of the model are as follows:

$$
{}_{Y_0}^{F}T = \begin{pmatrix} 1 & 0 & 0 & 0 \\ 0 & 1 & 0 & 0 \\ 0 & 0 & 1 & 0 \\ 0 & 0 & 0 & 1 \end{pmatrix}
\qquad\qquad \text{Equation 2}
$$

$$
{}_{Y_0'}^{Y_0}T = \begin{pmatrix} 1 & 0 & 0 & 0 \\ 0 & 1 & 0 & 0 \\ 0 & 0 & 1 & 0 \\ 0 & 0 & 0 & 1 \end{pmatrix}
\qquad\qquad \text{Equation 3}
$$

$$
{}_{Y}^{Y_0'}T = \begin{pmatrix} 1 & 0 & 0 & 0 \\ 0 & 1 & 0 & y \\ 0 & 0 & 1 & 0 \\ 0 & 0 & 0 & 1 \end{pmatrix}
\qquad\qquad \text{Equation 4}
$$

7

$$\substack{Y \\ Y'}T = \begin{pmatrix} & & & E_{XY} \\ & \left[R(\hat{k}_Y, E_{C(0Y)X})\right]_{3\times3} & & E_{YY} \\ & & & 0 \\ & 0_{1\times3} & & 1 \end{pmatrix}$$

Equation 5

$$\substack{Y' \\ X_0}T = \begin{pmatrix} 1 & 0 & 0 & 0 \\ 0 & 1 & 0 & 0 \\ 0 & 0 & 1 & 0 \\ 0 & 0 & 0 & 1 \end{pmatrix}$$

Equation 6

$$\substack{X_0 \\ X_0'}T = \begin{pmatrix} 1 & 0 & 0 & 0 \\ 0 & 1 & 0 & 0 \\ 0 & 0 & 1 & 0 \\ 0 & 0 & 0 & 1 \end{pmatrix}$$

Equation 7

$$\substack{X_0' \\ X}T = \begin{pmatrix} 1 & 0 & 0 & x \\ 0 & 1 & 0 & 0 \\ 0 & 0 & 1 & 0 \\ 0 & 0 & 0 & 1 \end{pmatrix}$$

Equation 8

$$\substack{X \\ X'}T = \begin{pmatrix} 1 & 0 & 0 & E_{XX} \\ 0 & 1 & 0 & E_{YX} \\ 0 & 0 & 1 & 0 \\ 0 & 0 & 0 & 1 \end{pmatrix}$$

Equation 9

$$\substack{X' \\ t}T = \begin{pmatrix} 1 & 0 & 0 & 0 \\ 0 & 1 & 0 & 0 \\ 0 & 0 & 1 & 0 \\ 0 & 0 & 0 & 1 \end{pmatrix}$$

Equation 10

$$\substack{t \\ t'}T = \begin{pmatrix} 1 & 0 & 0 & E_{Xt} \\ 0 & 1 & 0 & E_{Yt} \\ 0 & 0 & 1 & 0 \\ 0 & 0 & 0 & 1 \end{pmatrix}$$

Equation 11

where for instance $R(\hat{k}_Y, E_{C(0Y)X})$ depicts a rotation by an angle $E_{C(0Y)X}$ around the Z-axis of the Y-axis reference frame and E_{XY} and E_{YY} are straightness error motion of the Y-axis in the x-direction and linear positioning error of the Y-axis. Additionally, E_{XX}, E_{YX}, E_{Xt} and E_{Yt} are linear positioning error of the X-axis, straightness error motion of the X-axis in the y-direction, tool offset in the x-direction, and tool offset in the y-direction, respectively.

In the workpiece branch, the deviation of the actual position of the workpiece ball with respect to the foundation frame is:

$$\substack{\{F\},F \\ w'}P = \substack{F \\ w}T \substack{w \\ w'}T \begin{bmatrix} 0 & 0 & 0 & 1 \end{bmatrix}^T$$

Equation 12

However, since there is no physical means of distinguishing between the foundation frame and the actual workpiece ball position all HTMs in *Equation 12* are replaced by the identity matrix as only one setup is used and the workpiece ball is used as the foundation frame origin.

The LDBB readings, ρ, are computed by the subtraction of the nominal trajectory radius, R, from the actual cartesian distance between the actual positions of the tool and workpiece balls as follows:

$$\rho = R' - R \qquad \text{Equation 13}$$

where the actual cartesian distance is:

$$R' = \left\| {}^{\{F\},F}_{t}P - {}^{\{F\},F}_{w}P \right\| \qquad \text{Equation 14}$$

While the above model is theoretically exact for any size of deviations, a simplified linearized model can be produced assuming that deviations are small. This model can easily be solved to estimate the causal deviations indirectly from measurements of the volumetric errors. A geometric Jacobian matrix, J, propagates the causal geometric errors, E_G, which include the geometric errors occurring at the joints and the setup errors, to the volumetric cartesian errors, E_V, as follows [20]

$$E_V = J\, E_G \qquad \text{Equation 15}$$

where

$$J = \begin{bmatrix} x & 0 & y^2 & 0 & 0 & 1 & 0 \\ 0 & x^2 & 0 & y & x & 0 & 1 \\ 0 & 0 & 0 & 0 & 1 & 0 & 0 \end{bmatrix} \qquad \text{Equation 16}$$

where x and y are the joint coordinates for axis X and Y respectively. Each column of the Jacobian matrix is related to the following geometric errors and setup errors composing $E_G = [\,E_{XX1}, E_{YX2}, E_{XY2}, E_{YY1}, E_{C(0Y)X}, E_{Xt0}, E_{Yt0}\,]^T$.

Equation 15 can be contextualized to the telescopic loaded double ball bar reading by projecting the translational volumetric error vector along the sensitive direction of the ball bar at position i

$$\rho_{G,i} = J_{G,i}\, E_G \qquad \text{Equation 17}$$

where

$$J_{G,i} = [\cos\theta_i \ \ \sin\theta_i \ \ 0]\, J \qquad \text{Equation 18}$$

with θ_i being the angle that the ball-bar sensitive direction makes with the X-axis.

Multiple measurements around the circular trajectory are concatenated vertically to yield a single linear system relating all ball bar readings to the causal geometric errors occurring at the joint and the setup errors of the balls of the ball-bar

$$\rho_G = J_G \, E_G \qquad \text{Equation 19}$$

The compliance model calculates the deflection occurring at the tool relative to the workpiece due to a wrench applied between the tool and the workpiece in the presence of compliance (inverse of stiffness) at the joints. It requires calculating the reaction wrench at the joints, the resulting deflection at the joint, and propagating these deflections down the kinematic chains to the tool in the tool branch and the workpiece in the workpiece branch using the geometric Jacobian. For each measurement $i=1,m$ of the LDBB a wrench W_i is applied resulting in a change in the LDBB length $\rho_{C,i}$ as follows [18]:

$$\rho_{C,i} = \hat{B}^T{}_i \, J_i \, C_{\text{joint}} \, J^T{}_i \, W_i \qquad i = 1, m \qquad \text{Equation 20}$$

The authors did not find a closed-form solution for the compliance matrix from experimental measurements of the applied wrench and resulting LDBB length changes. Instead, *Equation 20* was used to generate a wrench Jacobian J_W which is introduced in [18].

3. Elasto-geometric model parameter estimation

Intuitively, the geometric errors will cause a certain change in the length of the loaded ball bar even if no load is applied. Then, by applying a controlled load the compliance within the system will result in an additional change in the ball bar length. As a result, the geometric effect does not cause a change in load and so the elasto-geometric model becomes

$$\rho_H = \rho_C + \rho_G \qquad \text{Equation 21}$$

where ρ_G, ρ_C and ρ_H are the ball-bar length change due to the geometric errors, the compliance deflection, and both (the letter H was chosen for hybrid compliance and geometric error model), respectively. Using data at a single force level is not likely to allow us to distinguish between the geometric and compliance error sources. Let us consider two force levels for the system of equations to separate parameters with an effect that is constant across force levels, i.e. geometric errors, from parameters that have an effect proportional to the applied force, i.e the compliances. For example, using two force levels and linearized wrench Jacobian which is introduced in [18], for each level yields *Equation 22* and *Equation 23*

$$\rho_{C,1,i} = J_{F,1,i}\, C \qquad \text{Equation 22}$$

$$\rho_{C,2,j} = J_{F,2,j}\, C \qquad \text{Equation 23}$$

which are then substituted in the combined equation

$$\rho_{H,1,i} = \rho_{C,1,i} + \rho_{G,i} \qquad \text{Equation 24}$$

$$\rho_{H,2,j} = \rho_{C,2,j} + \rho_{G,j} \qquad \text{Equation 25}$$

By substituting *Equation 17*, *Equation 22* and *Equation 23* in *Equation 24* and *Equation 25*,

$$\rho_{H,1,i} = J_{F,1,i}C + J_{G,i}\, E_{G} \qquad \text{Equation 26}$$

$$\rho_{H,2,j} = J_{F,2,j}C + J_{G,j}\, E_{G} \qquad \text{Equation 27}$$

which can be written in a matrix form,

$$\begin{bmatrix} \rho_{H,1,i} \\ \rho_{H,2,j} \end{bmatrix} = \begin{bmatrix} J_{F1,i} & J_{G,i} \\ J_{F2,j} & J_{G,j} \end{bmatrix} \begin{bmatrix} C \\ E_{G} \end{bmatrix} \qquad \text{Equation 28}$$

For $i=1$, m_1, and $j=1$ to m_2, there are $m=m_1+m_2$ measurements in total so *Equation 28* can be re-written

$$\begin{bmatrix} \rho_{H,1} \\ \vdots \\ \rho_{H,m} \end{bmatrix}_{m \times 1} = \begin{bmatrix} J_{F,1} & J_{G,1} \\ \vdots & \vdots \\ J_{F,m} & J_{G,m} \end{bmatrix}_{m \times 13} \begin{bmatrix} C \\ E_{G} \end{bmatrix}_{13 \times 1} \qquad \text{Equation 29}$$

Equation 29 can be summarized as follow:

$$\rho_{H_{m \times 1}} = J_{H_{m \times 13}} P_{H_{13 \times 1}} \qquad \text{Equation 30}$$

where, ρ_{H} is the summation of the compliance and geometric LDBB length change readings. J_{H} is the elasto-geometric Jacobian which is constituted by the combination of the wrench Jacobian and geometric Jacobian. Finally, P_{H} is the combined parameters set which are composed of compliance and geometric parameters. To estimate the elasto-geometric parameters, *Equation 30* is solved using the elasto-geometric Jacobian pseudoinverse as follows:

$$P_{H,est_{13 \times 1}} = J^{+}{}_{H_{13 \times m}}\, \rho_{H_{m \times 1}} \qquad \text{Equation 31}$$

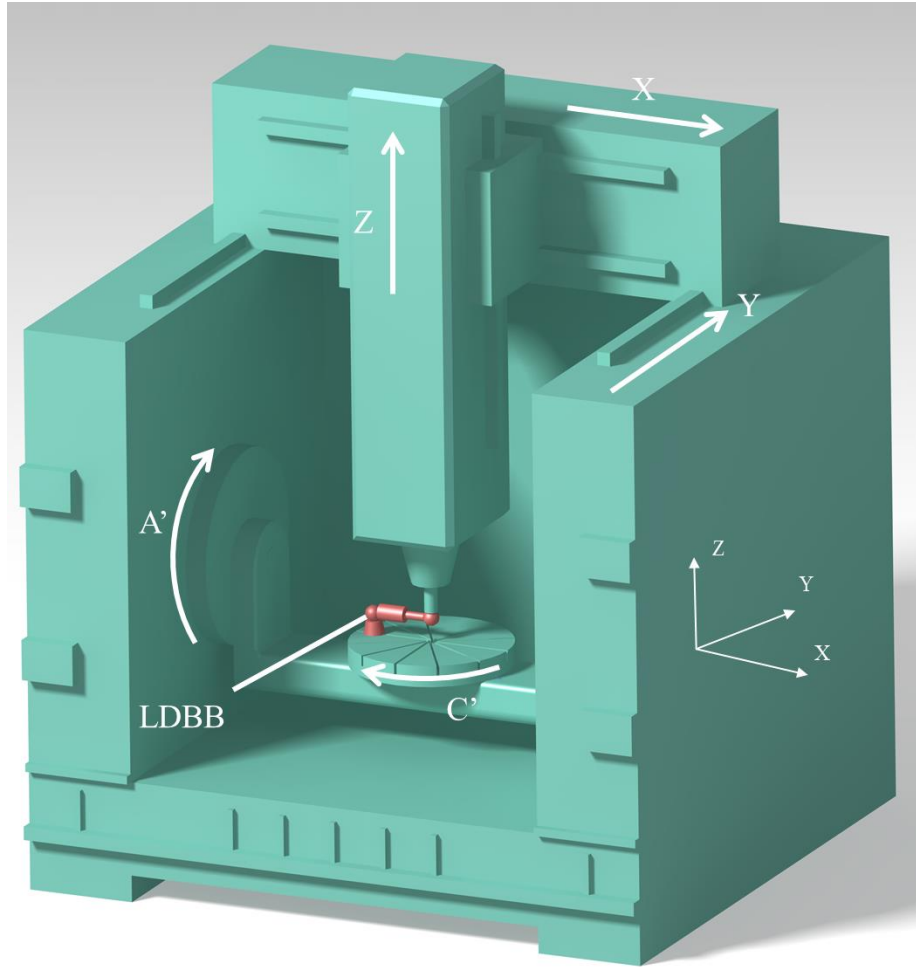*Fig. 2* shows a 3D rendering of the tested 5-axis CNC machine with the topology wCAFYXZSt.

Fig. 2. 3D rendering of the target 5-axis machine tool (wCAFYXZSt) with the LDBB mounted.

4. Simulation

Fig. 3 shows the data flow for the simulation of the elasto-geometric model. The joint compliances are simulated at reasonable values from the literature review. The simulated LDBB readings due to the compliance calculated with *Equation 20* and the simulated geometric contributions to the readings calculated with *Equation 13* geometric are summed up using *Equation 24* and *Equation 25* to generate the combined readings. In the estimation process *Equation 31* yields the estimated combined parameters (compliance and geometric parameters) which are then compared with the simulated values. They are also used back in *Equation 20* and *Equation 13* to predict the LDBB combined readings which are compared with the initially simulated readings.

Fig. 3. Data flow for the simulation of the elasto-geometric Model.
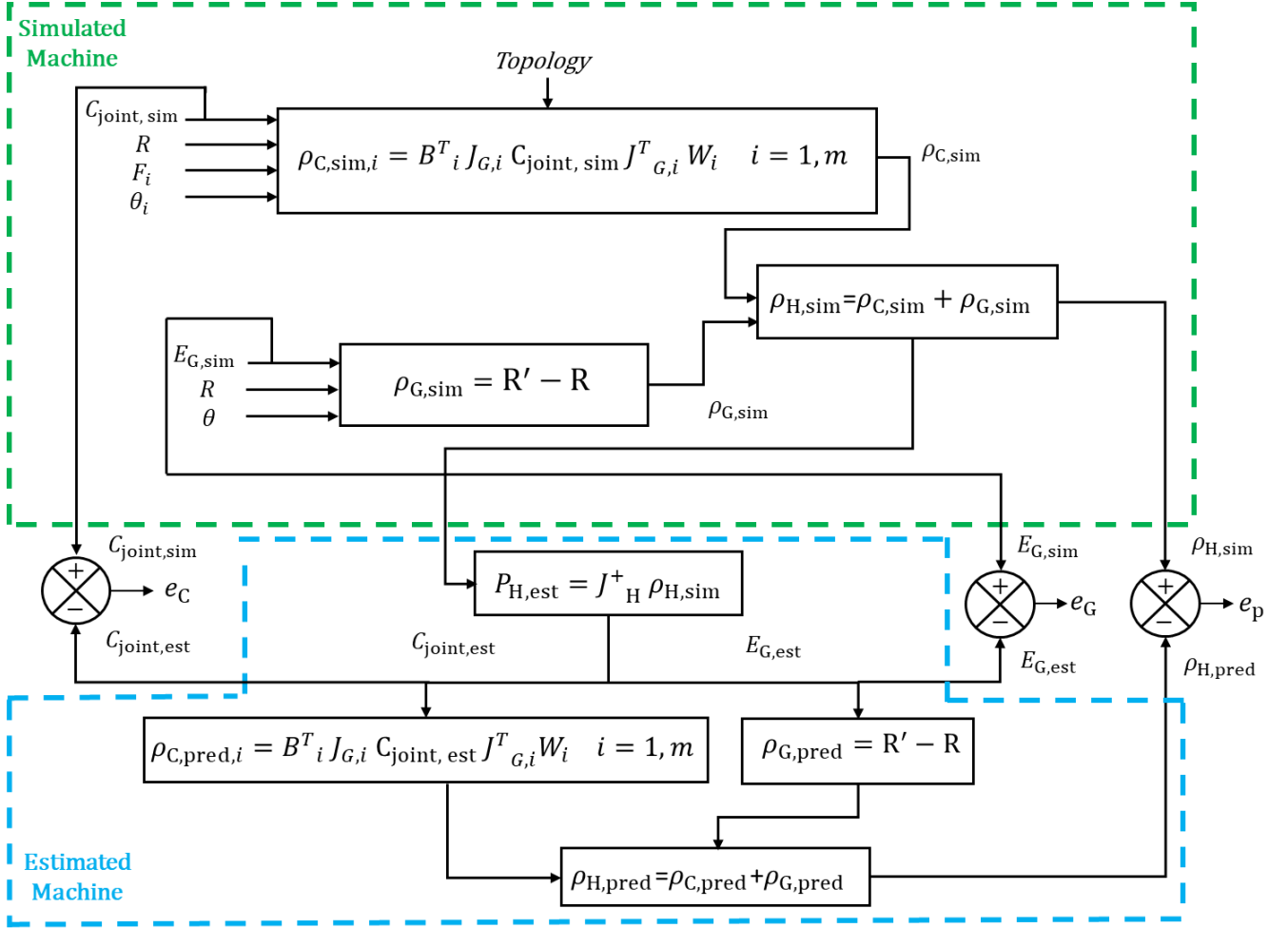
W: simulated wrench at the tool
F: loaded double ball bar force
R: nominal trajectory radius
R': Cartesian distance
θ: loaded double ball bar rotation angle
$C_{\text{joint,sim}}$: simulated compliance for each axis
$C_{\text{joint,est}}$: estimated compliance for each axis
$E_{\text{G,sim}}$: simulated geometric parameters for each axis
$E_{\text{G,est}}$: estimated geometric parameters for each axis
$\rho_{\text{G,sim}}$: simulated geometric loaded double ball bar reading
$\rho_{\text{C,sim}}$: simulated compliance loaded double ball bar reading
$\rho_{\text{H,sim}}$: elasto-geometric (combined) simulated loaded double ball bar reading
$\rho_{\text{H, pred}}$: elasto-geometric (combined) predicted loaded double ball bar reading
J_{H}: elasto-geometric (combined) Jacobian matrices
$\rho_{\text{C,pred}}$: predicted compliance loaded double ball bar reading
$\rho_{\text{G,pred}}$: predicted geometric loaded double ball bar reading
e_{G}: geometric parameters error
e_{C}: compliance error
e_{P}: loaded double ball bar reading error

Since only the X- and Y-axis of the wCAFYXZSt machine, illustrated in *Fig. 2*, are engaged in the 2D circular test only compliance and geometric errors in the XY plane and rotations around the Z-axis are considered. As a result, the model may use those modeled axes to explain effects, which may in reality originate from non-modeled axes of the real machine. The following relevant geometric errors for the 2D test as shown in *Fig. 1,* are simulated: E_{XX1}, E_{YX2}, E_{XY2}, E_{YY1}, $E_{C(0Y)X}$, E_{Xt0} and E_{Yt0}. They are described in *Table 1*.

The linearized wrench Jacobian matrix which is introduced in [18] has 18 columns, which represent each compliance term. The condition number and rank of the wrench Jacobian matrix are 1.7e+34 and six, respectively. The rank of the matrix shows that there are only six independent columns out of 18. Twelve compliances must be removed from the estimation process. If the numerical Jacobian matrix has identical or linearly related columns, one of the compliances associated with this set is kept and the others are removed. *Table 2* lists such compliance sets of confounded compliances. Compliances associated with null columns are also removed. The retained compliances as shown in *Fig. 1*, are C_{XXX}, C_{XYX}, C_{YYY}, C_{CXY}, C_{CYY} and C_{CCY} which are in bold in *Table 2*. However, other compliances from each confounded set could have been selected. The reduced Jacobian condition number decreases to 9742 while the rank remains at six. The detailed descriptions of the kept compliance and geometric parameters are presented in *Table 1*.

Table 1. A detailed description of relevant compliance and geometric errors

Error description	Symbol
Compliance causing a translation in x for a force in x at joint X	C_{XXX}
Compliance causing a translation in x for a force in y at joint X	C_{XYX}
Compliance causing a translation in y for a force in y at joint Y	C_{YYY}
Compliance causing a rotation around z (C) for a force in x at joint Y	C_{CXY}
Compliance causing a rotation around z (C) for a force in y at joint Y	C_{CYY}
Compliance causing a rotation around z (C) for a moment of the force around z (C) at joint Y	C_{CCY}
Linear positioning error gain of the X-axis	E_{XX1}
Quadratic straightness error motion of the X-axis in the Y-direction	E_{YX2}
Quadratic straightness error motion of the Y-axis in the X-direction	E_{XY2}
Linear positioning error gain of the Y-axis	E_{YY1}
Out-of-squareness of the X-axis relative to the Y-axis	$E_{C(0Y)X}$
Tool offset in the X-direction	E_{Xt0}
Tool offset in the Y-direction	E_{Yt0}

Compliances and geometric errors are individually simulated to detect similarities in the response of the LDBB. Parameters producing similar responses cannot be separated mathematically. LDBB response patterns generated by each compliance term are shown explicitly in [18] and reproduced in *Table 2*. *Table 3* presents the LDBB response patterns generated by each geometric term. According

to *Table 2* and *Table 3* all patterns of the compliance except C_{CCY} are also found in the geometric error table. However, the model assumes that the patterns from geometric errors do not change size with the load whereas those due to load and compliance will. As a result, by feeding the estimation model with data taken at least for two load levels the two sources of errors should be separable.

Table 2. LDBB response patterns generated by each compliance term (one unit of the radial scale represents 15.0 µm) [18].

List of compliances and their corresponding LDBB patterns (kept compliances are in bold)	
$\boldsymbol{C_{XXX}}$, C_{XXY}	C_{XCY}, $\boldsymbol{C_{CXY}}$
$\boldsymbol{C_{XYX}}$, C_{YXX}, C_{XYY} , C_{YXY}	C_{YCY}, $\boldsymbol{C_{CYY}}$
C_{YYX}, $\boldsymbol{C_{YYY}}$	$\boldsymbol{C_{CCY}}$

16

Table 3. LDBB response patterns generated by each geometric error parameter (one unit of the radial scale represents 15.0 µm).

List of geometric parameters each producing the pattern shown			
E_{XX1}	E_{YX2}	E_{XY2}	E_{YY1}
$E_{C(0Y)X}$	E_{Xt0}	E_{Yt0}	-

.
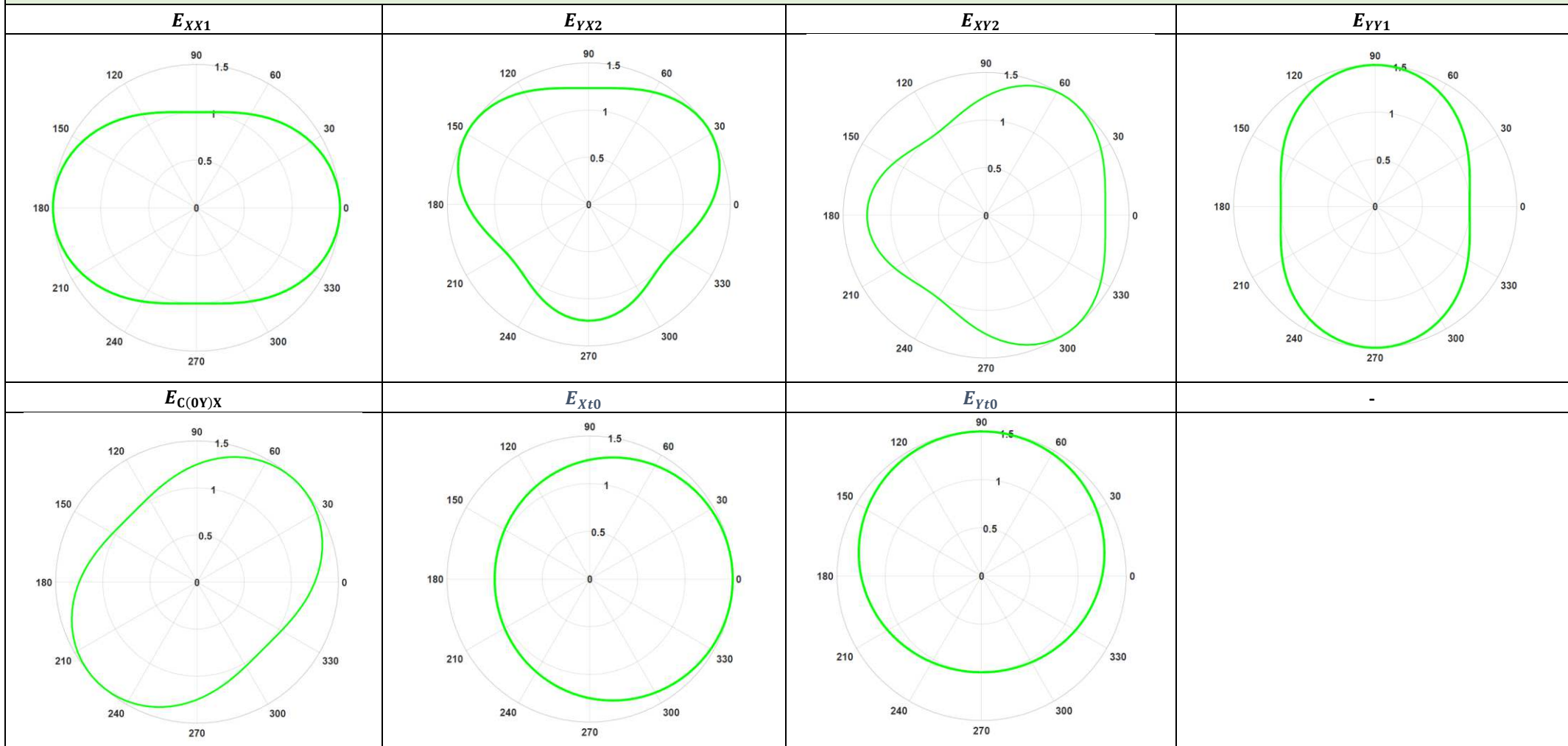
Some simulations are also conducted to show that although some geometric and compliance parameters produce similar patterns the size of the compliance pattern varies with the applied force thus allowing its separation from the geometric effect. For this simulation E_{XX1} and C_{XXX} are set to 1.1200 E-04 and 1.1000 E-04, respectively, and seven force values are simulated i.e., 36,112, 238, 364, 490, 616, and 742 N. The LDBB readings are shown in *Fig. 4*. At a force of 0 N, the compliance does not contribute to the LDBB readings and so only the geometric error produces the response. As shown in *Fig. 4,* for non-zero forces from 36 to 742 N the readings gradually increase. Both C_{XXX} and E_{XX1} cause an ovalisation of the response along the X-axis but the size of the oval effect due to the compliance parameters changes with the applied force whereas the geometric effect, as modeled, does not.
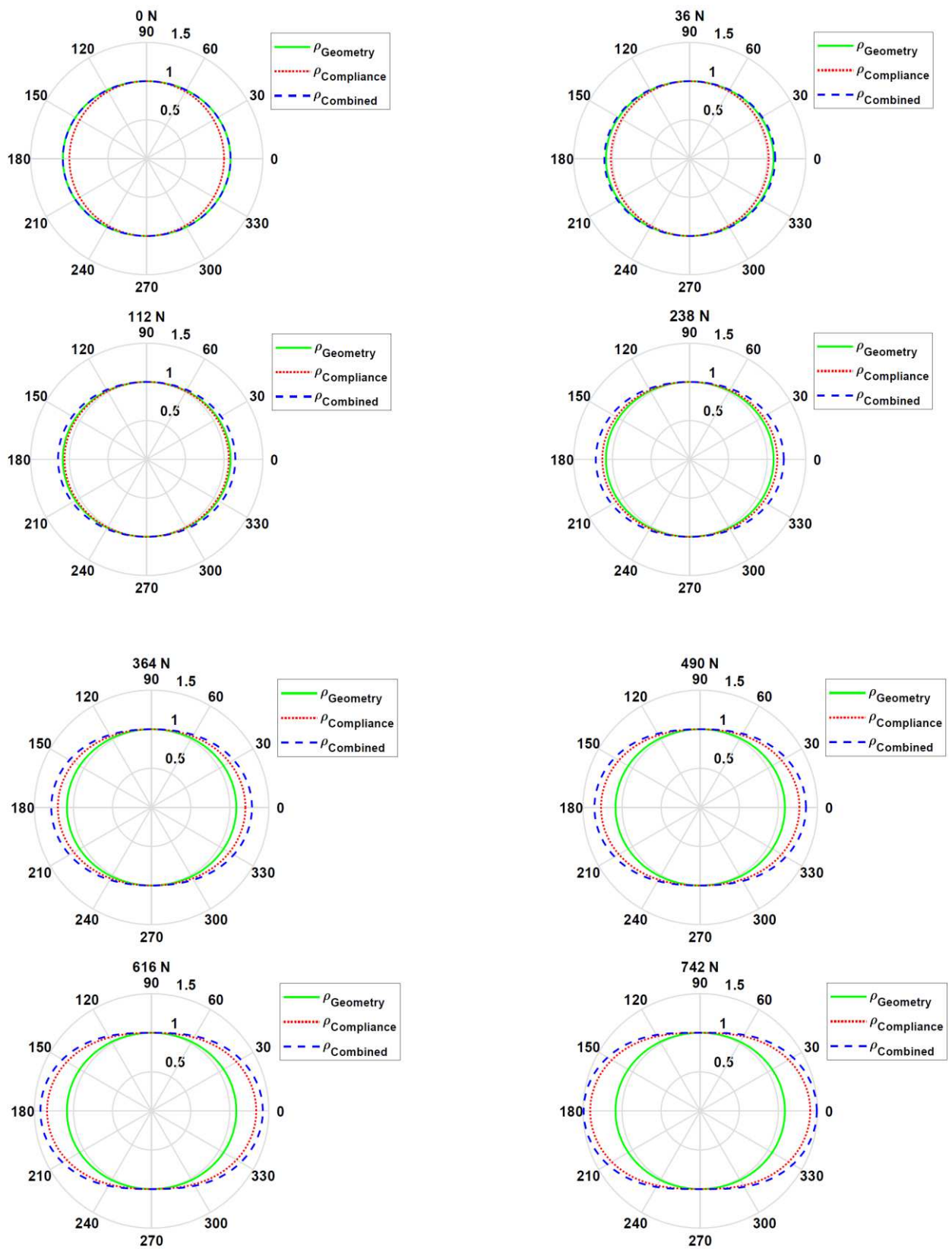
Fig. 4. The LDBB's simulated as well as integrated compliance and geometric readings with a given value of C_{XXX} and E_{XX1} for seven different force levels (36,112, 238, 364, 490, 616 and 742 N).

Table 4. Simulated and estimated compliance values and geometric errors

Error	Simulated	Estimated	Difference	% Difference
E_{XX1}	1.1200E-04	1.1200E-04	0.0000	0.0000
E_{YX2}	1.2300E-07	1.2295E-07	5E-11	0.0406
E_{XY2}	-2.1300E-06	-2.1305E-06	5E-10	-0.0234
E_{YY1}	-2.2000E-04	-2.2195E-04	-1.95E-06	0.8863
$E_{C(0Y)X}$	2.6100E-05	2.6097E-05	-3E-09	-0.0114
E_{Xt0}	6.1100E-04	6.1179E-04	7.9E-07	0.1292
E_{Yt0}	6.2200E-04	6.2196E-04	-4E-08	-0.0064
C_{XXX}	1.1000E-04	1.1000E-04	0.0000	0.0000
C_{XYX}	1.2000E-04	1.2000E-04	0.0000	0.0000
C_{YYY}	5.5000E-04	5.5000E-04	0.0000	0.0000
C_{CXY}	6.4000E-06	6.4000E-06	0.0000	0.0000
C_{CYY}	6.5000E-06	6.5000E-06	0.0000	0.0000
C_{CCY}	6.6000E-08	6.5999E-08	-1E-12	-0.0015

Fig.5 shows the simulated and predicted LDBB readings for the simulated and estimated model parameter values in *Table 4*. Simulated and estimated values are close to each other. As shown in *Fig.5*, the simulated and predicted readings are similar.
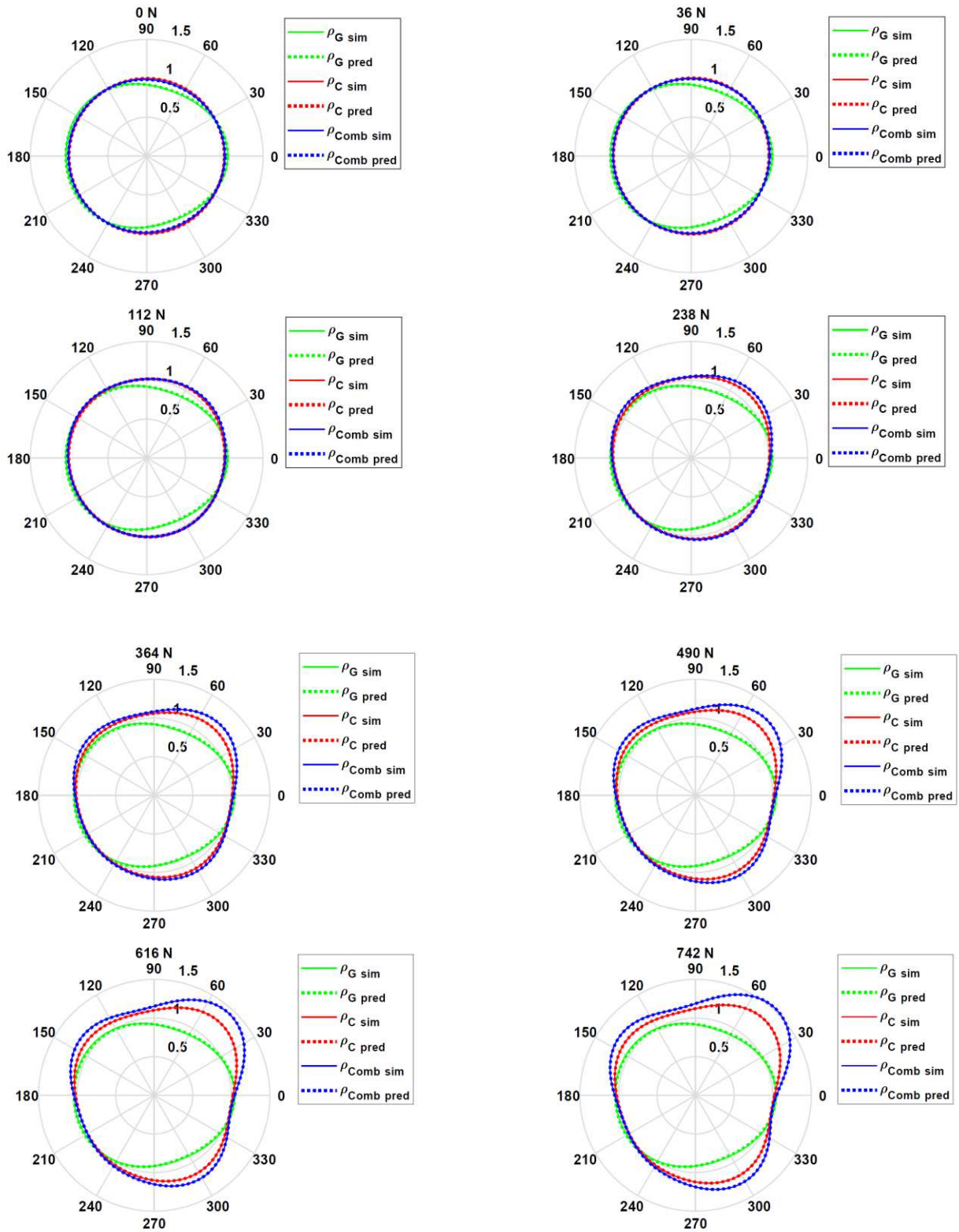
Fig.5. Simulated and predicted LDBB readings for values listed in *Table 4* for eight different force levels (0, 36,112, 238, 364, 490, 616, and 742 N). $\rho_{\text{G sim}}$, $\rho_{\text{C sim}}$, $\rho_{\text{Comb sim}}$, $\rho_{\text{G pred}}$, $\rho_{\text{C pred}}$ and $\rho_{\text{Comb pred}}$ is the simulated geometric, compliance, combined and predicted geometric, compliance, and combined readings respectively.

5. Experimental Results and discussion

Fig. 6 shows the loaded double ball bar test setup. A loaded double ball bar applies a controlled radial force between the work table and the tool holder of a machine tool while measuring the radial deviations during a circular path on a machine tool. The test is conducted on a machine tool with the configuration wCAFYXZt. The LDBB has a length of 150 mm, and the test feed rate is 2000 mm/min. The circular trajectory is in the XY plane with starting and ending angles of $0°$ and $360°$, respectively. Radial displacement readings are measured for seven tests at forces of 36, 112, 238, 364, 490, 616, and 742N corresponding to pressure levels of 0.4, 1, 2, 3, 4, 5, and 6 bars internally applied to the LDBB through the pneumatic actuator, respectively. The radial displacement readout has a 0.00024 mm resolution. The raw data which was captured by the LDBB and readings were compensated for the setup deflection by using *Equation 32* [21]:

$$\delta = P \times 2.33 \times cos^2\theta \qquad \text{Equation 32}$$

where δ (µm), P (bar), and θ (degree) are the deflection at the workpiece ball, the air pressure, and the angle of the LDBB with the horizontal plane, respectively. The LDBB is perpendicular to the horizontal plane, therefore $\theta = 0$ degree.

Both the tool and the workpiece balls have a radius of 30 mm. According to ISO 3290-1:2014 [22], spheres of that radius can be reasonably well produced up to grade G20, i.e., with a tolerance in diameter of $\pm$ 11.5 µm; alternatively, the American Bearing Manufacturers Association standard defines tolerances of $\pm$12.5 µm for a corresponding grade G25 sphere. The LDBB measurement instrument features steel spheres for general industrial use. Thus, it must be assumed that each measurement contains an error component that is attributable to the imperfect shape of the sphere. It is possible to manufacture spheres according to much tighter roundness tolerance, e.g., the IBS Spindle Error Analyzer® features spheres with a roundness of less than $\pm$ 25nm [23]. The use of such spheres can reduce the complexity of understanding the measurement data as well as the time required to perform a measurement. Alternatively, one needs to employ error separation methods such as the Ball Reversal Method to quantify the contribution of the sphericity on the measurand [24]. For the work described in this manuscript, the form error of the spheres has not been compensated for. Based on the CMM measurement of these spheres, their form errors may contribute at most 30 µm. This means, that the model inaccurately re-attributes this error to the described kinematic machine tool errors. Nevertheless, this does not affect the modeling approach, as the measurement data, in general, should be compensated for this error before the model parameter estimation. In the analysis

of experimental results global and local methods have been used. In the global procedure, the data from all tested load levels are fed to the estimator. However, in the local method, reading from only two adjacent force levels is used to analyze the local compliance and geometric error parameters.
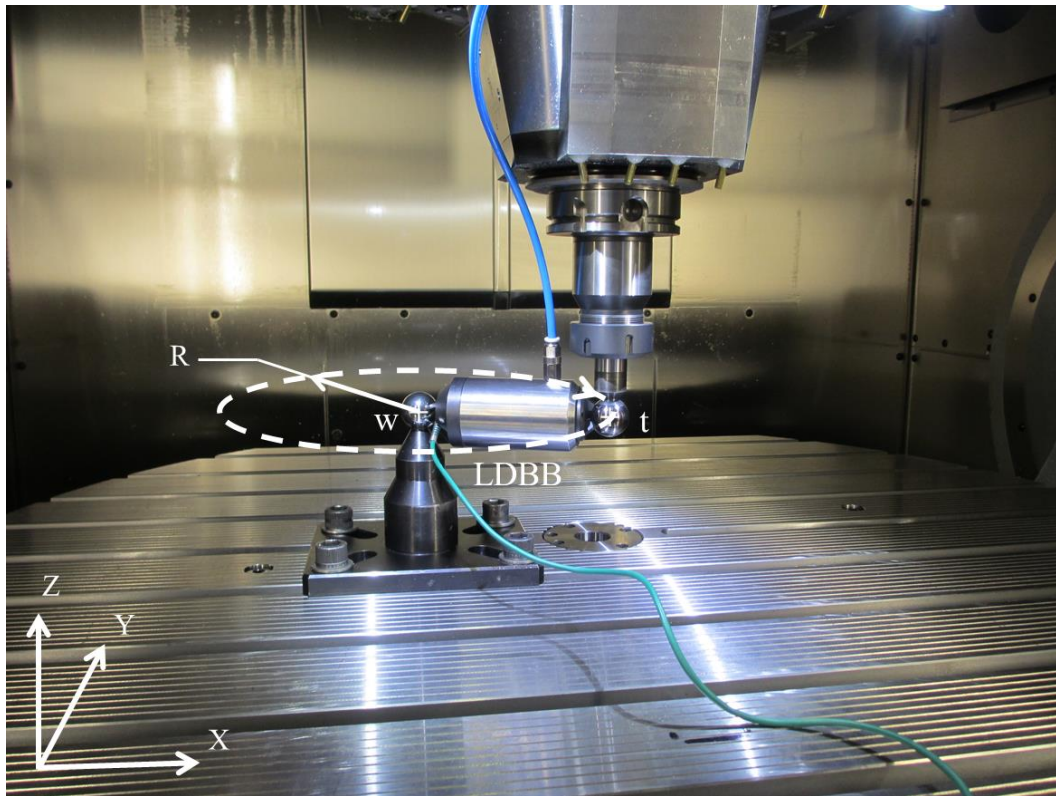

Fig. 6. Loaded double ball bar test setup. The direction of the test is clockwise. The work ball is fixed, and the tool ball is moving. The test is conducted in the XY plane.

5.1. Global (overall) compliance and geometric parameters

Using the results from all force levels at once in *Equation 31* yields global estimates for the compliance and geometric parameters. The estimated compliance and geometric parameters values are listed in *Table 5* and *Table 6*, respectively.

Table 5. Estimated global compliance value (mm/N) of X- and Y-axis using all force data at once.

		$C_{X\text{Estimated}}$ and $C_{Y\text{Estimated}}$					
		Wrench					
		F_{XX}	F_{YX}	M_{CX}	F_{XY}	F_{YY}	M_{CY}
Twist	δ_{XX}	6.19E-05	7.98E-07	0	0	0	0
	δ_{YX}	0	0	0	0	0	0
	δ_{CX}	0	0	0	0	0	0
	δ_{XY}	0	0	0	0	0	0
	δ_{YY}	0	0	0	0	4.61E-05	0
	δ_{CY}	0	0	0	-2.69E-08	-1.66E-08	-1.10E-09

Table 6. Estimated global geometry value (rad, mm, or mm/m) of X- and Y-axis using all pressure data at once.

E_{XX1}	E_{YX2}	E_{XY2}	E_{YY1}	$E_{C(0Y)X}$	E_{Xt0}	E_{Yt0}
-0.00013	4.34E-07	-7.26E-07	-9.86E-05	1.15E-06	0.003891	-0.00062

Fig.7 shows the experimental and the model prediction of the loaded telescopic double ball-bar from 36 to 742 N force levels. The estimation is conducted without the 112 N dataset, which will be studied in the next section as it exhibits a non-linear behavior. As expected, the loaded telescopic double ball-bar readings increase with the applied force. Also, although the shape of the trace predicted generally follows the contour of the measurements there is a cyclical difference between them.
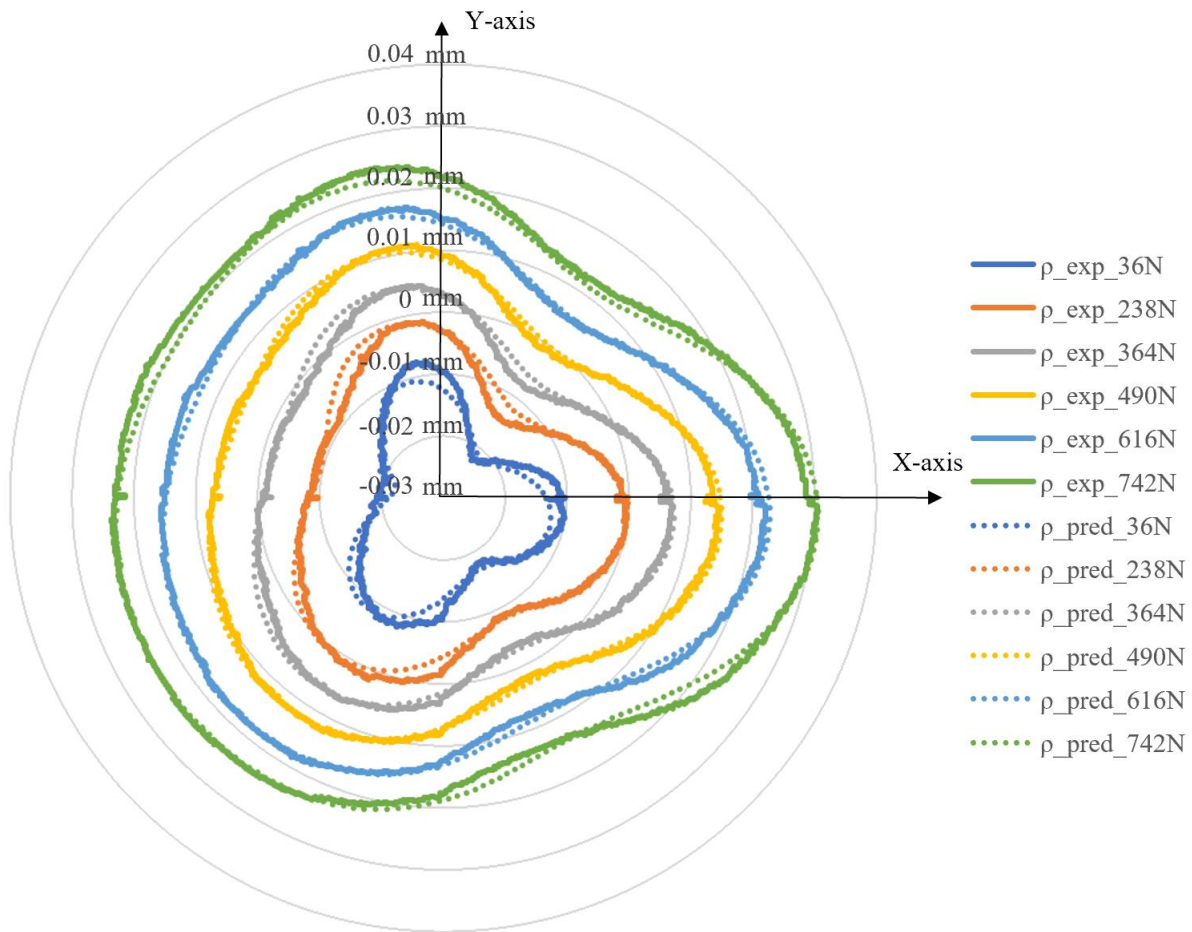
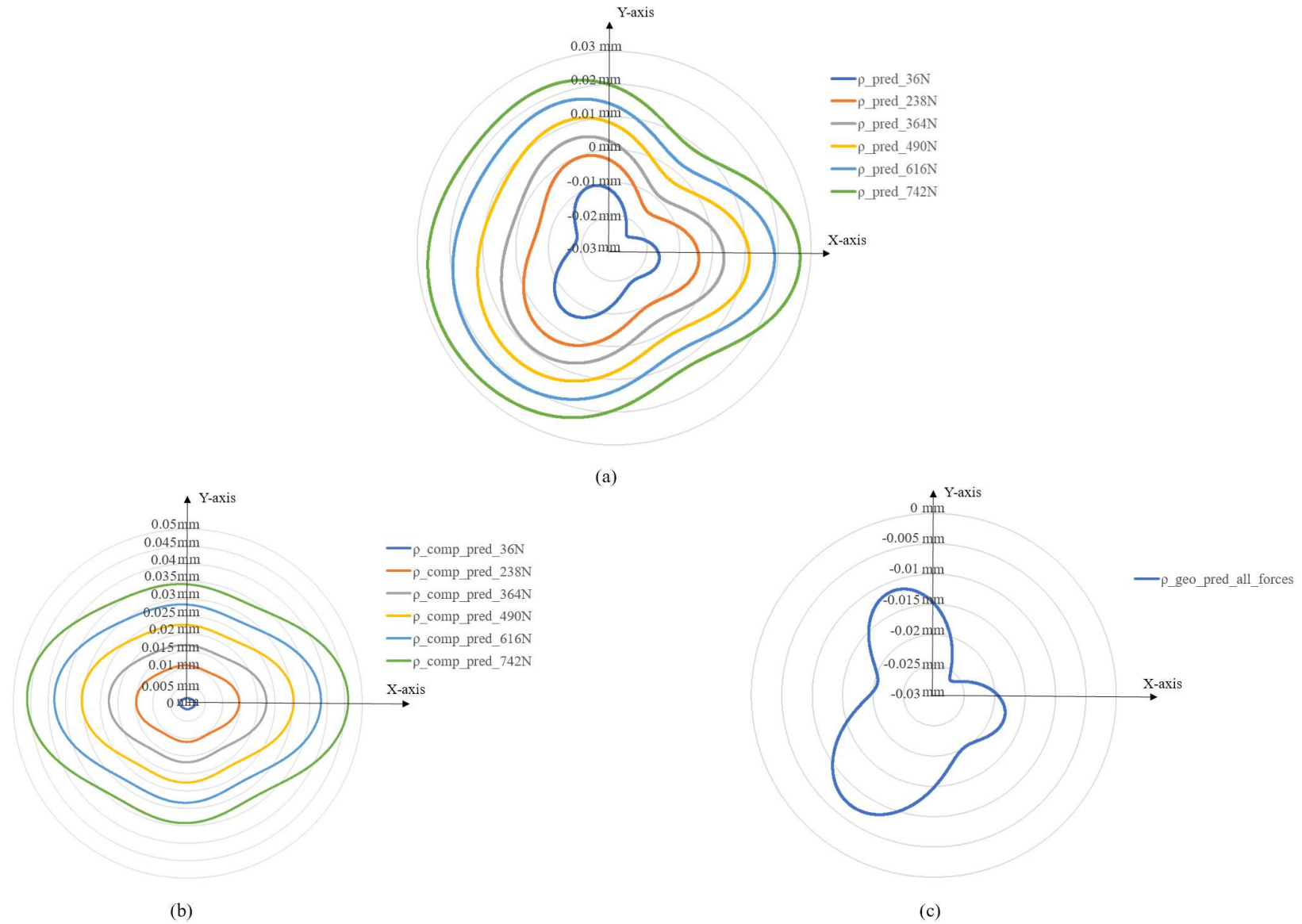Fig.7. Experimental and predicted global loaded double ball bar readings for X and Y-axis simultaneously with seven different levels of applied force. ρ_exp and ρ_pred are the experimental and predicted readings of a loaded double ball bar.

The model allows studying the relative contribution of the geometric and compliance parameters to the response. *Fig.8* shows the predicted readings in the absence of set-up errors (E_{Xt0} and E_{Yt0}) for (a) all compliance and geometric parameters, (b) the compliance parameters only, and (c) the geometric parameters only. Since the geometry of the machine is modeled as invariant with a load, all the predicted loaded geometric readings are identical. In *Fig.8 (b)* the maximum and minimum predicted radial LDBB readings attributed to the compliance are 0.046 and 0 mm, respectively, which results in a 0.046 mm radial variation. In *Fig.8 (c)* the maximum and minimum predicted radial LDBB readings due to the estimated geometric errors are -0.007 mm and -0.026 mm, respectively, which results in a 0.019 mm departure from the nominal circular trajectory. The radial variation due to compliance effects is more than 3 times that of geometric errors.

Fig. 9 and *Fig. 10* present predicted readings of the loaded double ball bar from the estimated global compliance and geometric parameters at the highest force (742 N), respectively. In *Fig. 9 (a)* the

impact of dominant equivalent compliance C_{XXX} and C_{YYY} on the loaded circular test readings are predicted to be around 0.045 and 0.034 mm peak-to-peak. In *Fig. 9 (b)* the impact of non-dominant equivalent compliances C_{XYX}, C_{CXY}, C_{CYY} and C_{CCY} are predicted to be around 0.00058, 0.0022, 0.0014 and 0.0045 mm peak-to-peak.

In *Fig. 10 (a)* the impact of dominant loaded geometric parameters E_{XX1} and E_{YY1} impact on the loaded circular test readings is predicted to be around 0.019 and 0.014 mm peak-to-peak. In *Fig. 10 (b)* the impact of loaded geometric parameters E_{YX2}, E_{XY2}, $E_{C(0Y)X}$, E_{Xt0} and E_{Yt0} are predicted to be around 0.0074, 0.012, 0.00017, 0.0076 and 0.0012 mm peak-to-peak.

Fig.8. Predicted global loaded double ball bar readings for the X and Y-axis simultaneously with seven different levels of applied force. (a) Predicted combined readings (ρ_pred). (b) Predicted compliance readings (ρ_comp_pred). (c) Predicted geometric readings (ρ_geo_pred).
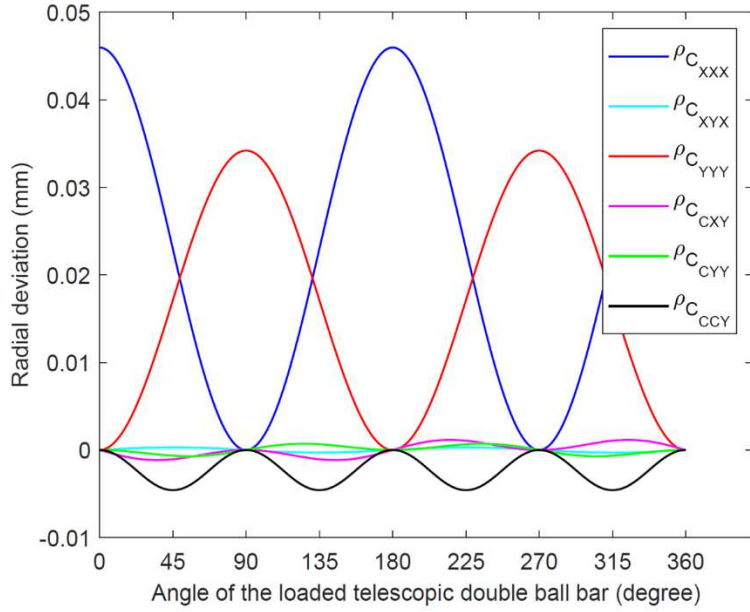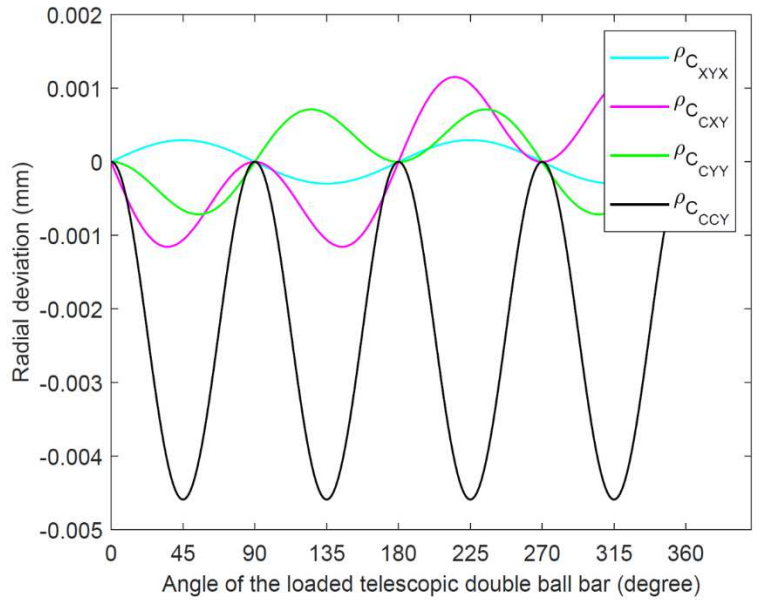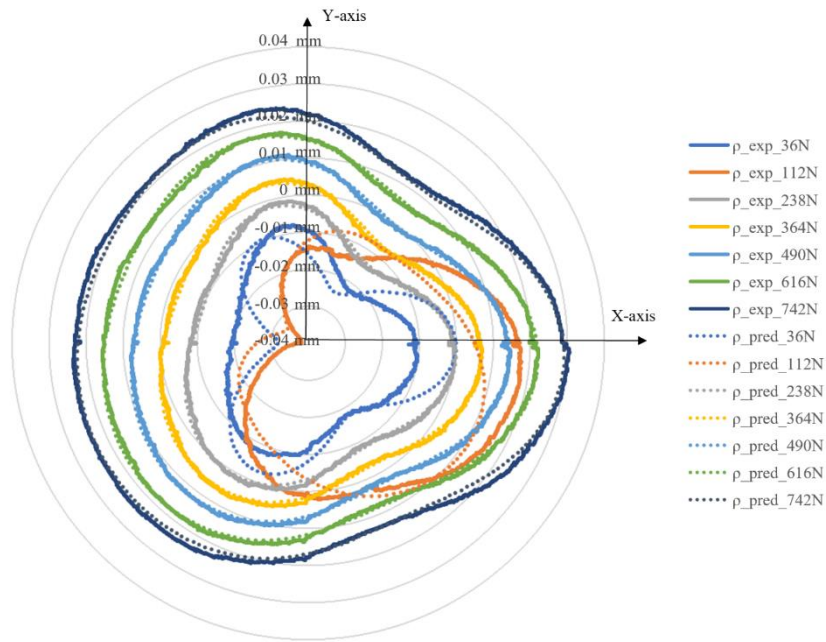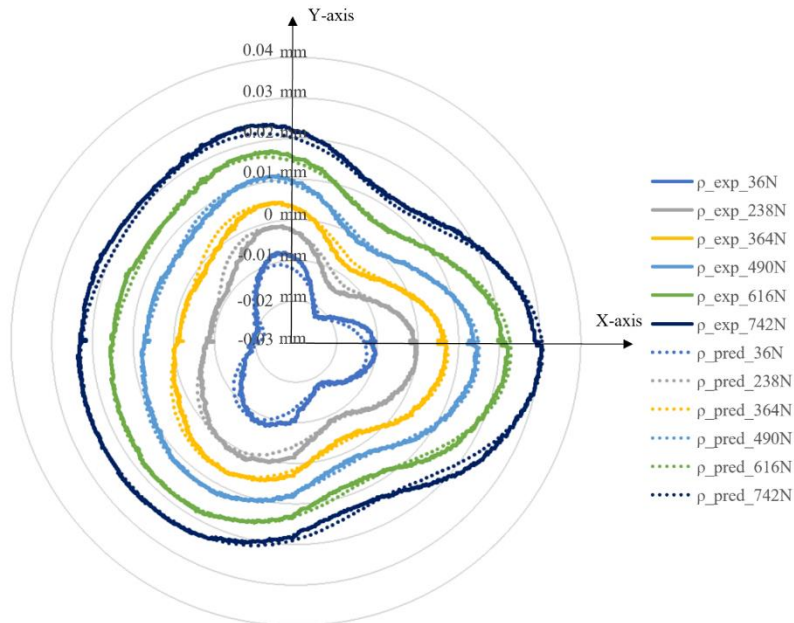
Fig. 9. Predicted readings of the loaded double ball bar (radial deviation versus the angle of the ball bar with the X-axis during the circular test) from the estimated global compliance parameters at the highest force (742 N). (a) C_{XXX}, C_{XYX}, C_{YYY}, C_{CXY}, C_{CYY} and C_{CCY}. (b) Only C_{XYX}, C_{CXY}, C_{CYY} and C_{CCY}.
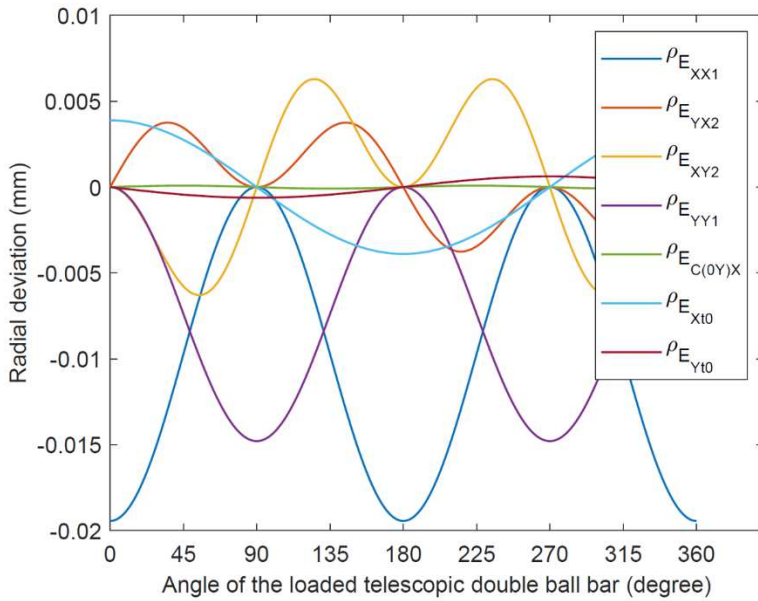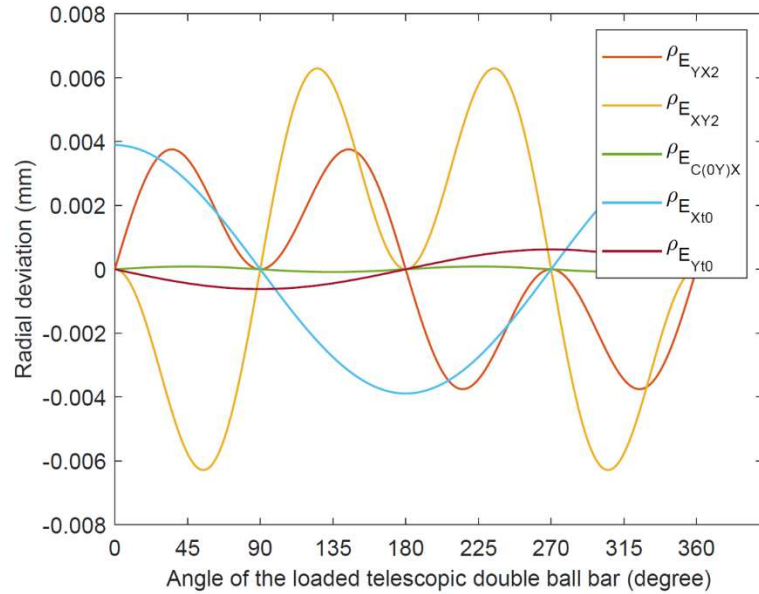
Fig. 10. Predicted readings of the loaded double ball bar (radial deviation versus the angle of the ball bar with the X-axis during the circular test) from the estimated global constant geometric parameters at the highest force (742 N). (a) E_{XX1}, E_{YX2}, E_{XY2}, E_{YY1}, $E_{C(0Y)X}$, E_{Xt0} and E_{Yt0}. (b) Only E_{YX2}, E_{XY2}, $E_{C(0Y)X}$, E_{Xt0} and E_{Yt0}.

28

5.2. Local compliance and geometric parameters

By using only two adjacent force levels: [36 and 112; 112 and 238; 238 and 364; 364 and 490; 490 and 616; 616 and 742] N a set of local compliance and geometric parameters are estimated. The experimental and predicted readings for a particular set of forces are illustrated in *Fig. 11(a).* From 238 N force, the predicted readings more closely follow the experimental readings. At 112 N force, results do not follow the general trend. This set of data significantly affects the estimated parameters and was removed for model estimation.

(a)

(b)

Fig. 11. Experimental and predicted local loaded telescopic double ball bar readings for X and Y-axis simultaneously with seven different levels of applied force. ρ_exp and ρ_pred are the experimental and predicted readings of a loaded telescopic double ball bar. (a) Includes the 112 N force level results and the predicted traces are obtained using parameters estimated using the following two adjacent force levels ([36, 112], [112, 238], etc.). (b) Without 112 N force level and using the following two adjacent force levels ([36, 238], [238, 364], etc.).

Fig. 12 shows the predicted local loaded telescopic double ball bar readings calculated using the estimated machine parameters, excluding the tool offsets. Three simulations are conducted: (a)

compliance and geometric parameters; (b) compliance parameters only and (c) geometric parameters only. Although theoretically unexpected the estimated geometry changes with force levels. A possible explanation is that the compliance model cannot fully explain the change in response and so the geometric errors are used to explain those effects. The predicted LDBB reading variation due to geometry variation is at most 0.0085 mm over the force range. This compares with 0.019 mm attributed to the global geometry obtained when using all force data at once. So the variation is early half the global value, which is not negligible. However, the overall shape of the geometric effect remains similar.

Fig. 13 and *Fig. 14* present predicted readings of the loaded double ball bar from the estimated local compliance and geometric parameters at the highest force (742 N), respectively. In *Fig. 13 (a)* the dominant equivalent compliance (C_{XXX}, C_{YYY}) impact on the loaded circular test readings are predicted to be around 0.048 and 0.036 mm peak-to-peak. In *Fig. 13 (b)* the impact of non-dominant equivalent compliances (C_{XYX}, C_{CXY}, C_{CYY} and C_{CCY}) are predicted to be around 0.0018, 0.0064, 0.001 and 0.0036 mm peak-to-peak.

In *Fig. 14 (a)* the loaded geometric parameters (E_{XX1}, E_{YY1}) impact on the loaded circular test readings is predicted to be around 0.022 and 0.017 mm peak-to-peak. In *Fig. 14 (b)* the impact of loaded geometric parameters (E_{YX2}, E_{XY2}, $E_{C(0Y)X}$, E_{Xt0} and E_{Yt0}) are predicted to be around 0.012, 0.014, 0.00082, 0.0068 and 0.0031 mm peak-to-peak.
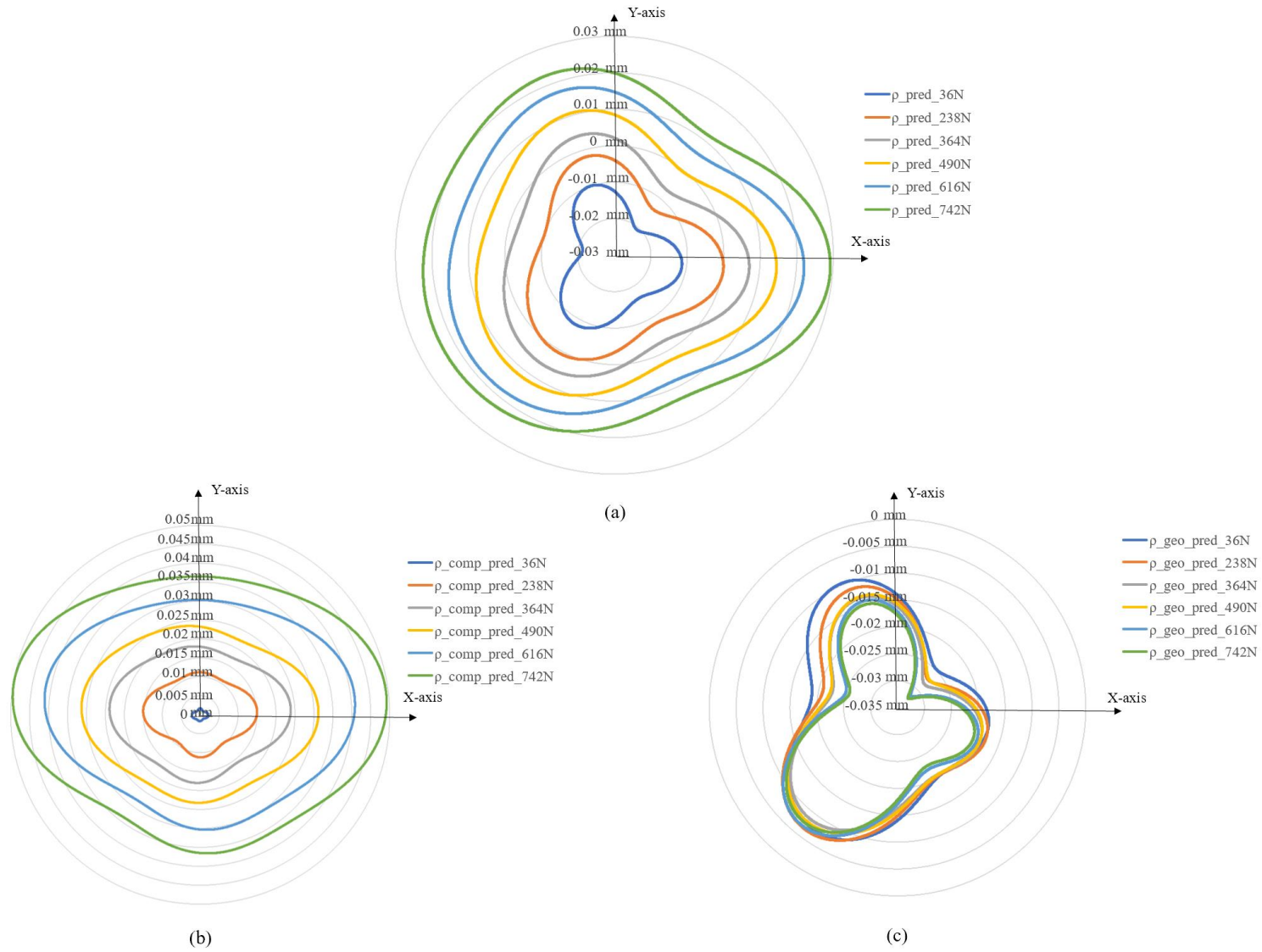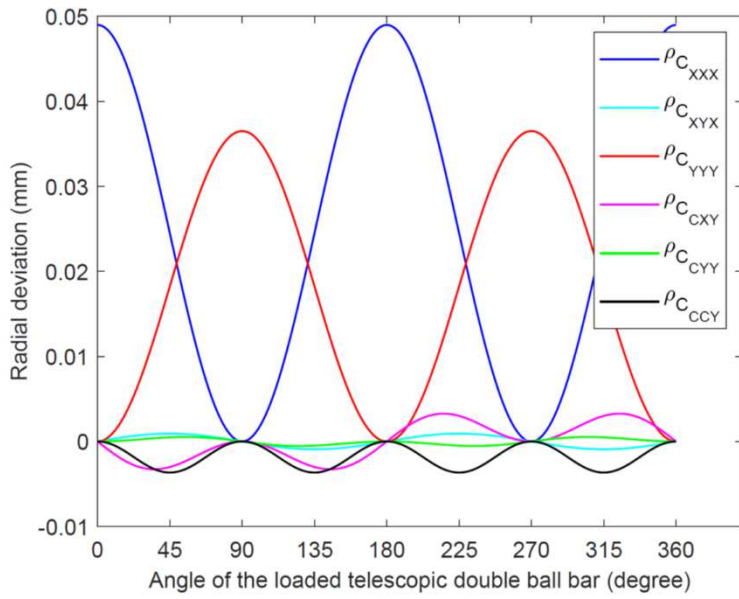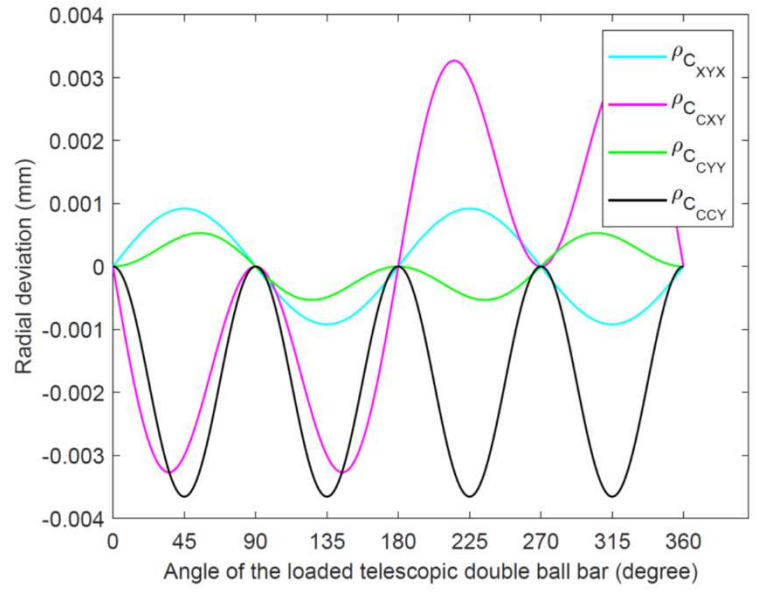
Fig. 12. Predicted local loaded telescopic double ball bar readings for the X and Y-axis simultaneously with seven different levels of applied force. (a) Predicted local combined readings (ρ_pred). (b) Predicted local compliance readings (ρ_comp_pred). (c) Predicted local geometric readings (ρ_geo_pred).
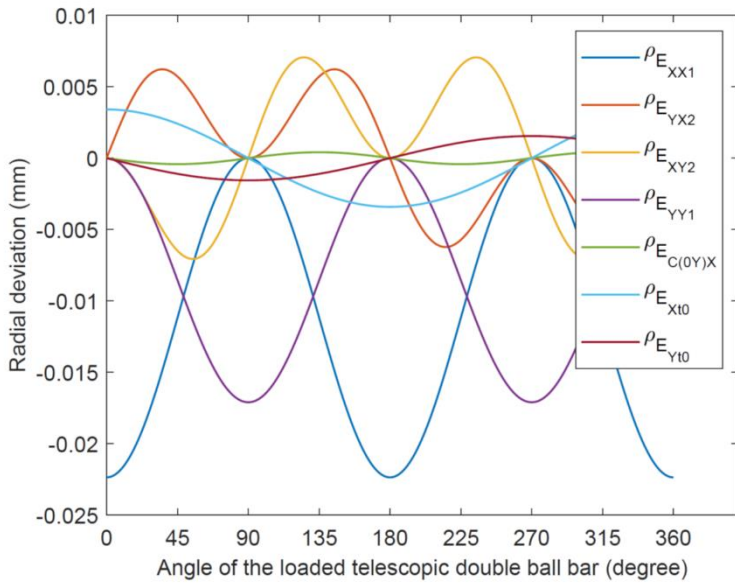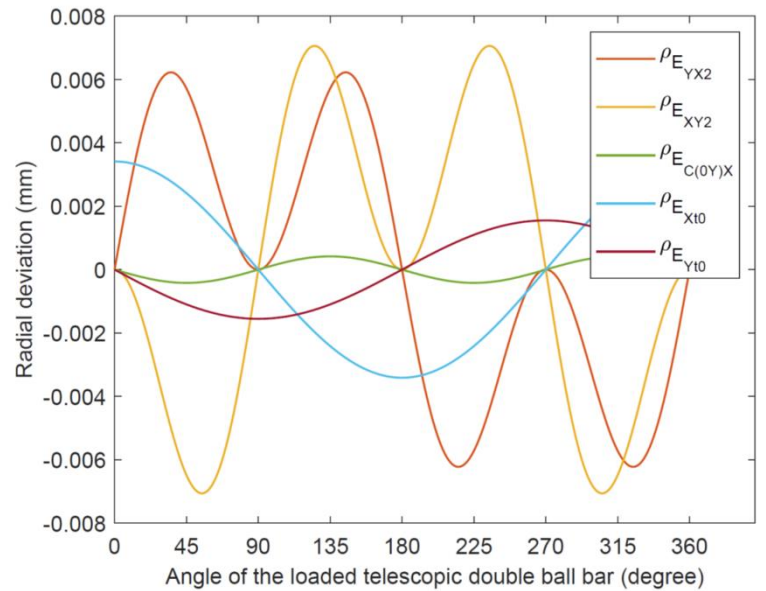
Fig. 13. Predicted readings of the loaded double ball bar (radial deviation versus the angle of the ball bar with the X-axis during the circular test) from the estimated local compliance parameters at the highest force (742 N). (a) C_{XXX}, C_{XYX}, C_{YYY}, C_{CXY}, C_{CYY} and C_{CCY}. (b) C_{XYX}, C_{CXY}, C_{CYY} and C_{CCY}.

Fig. 14. Predicted readings of the loaded double ball bar (radial deviation versus the angle of the ball bar with the X-axis during the circular test) from the estimated local geometric parameters at the highest force (742 N). (a) E_{XX1}, E_{YX2}, E_{XY2}, E_{YY1}, $E_{C(0Y)X}$, E_{Xt0} and E_{Yt0}. (b) E_{YX2}, E_{XY2}, $E_{C(0Y)X}$, E_{Xt0} and E_{Yt0}.

Error! Not a valid bookmark self-reference. and *Table 8* list the estimated local compliance and geometric parameters values.

Table 7. Estimated local compliances values (mm/N, rad/N or $\mathrm{rad}/\mathrm{N\ mm}$) for different sets of two force levels.

Force (N)	C_{XXX}	C_{XYX}	C_{YYY}	C_{CXY}	C_{CYY}	C_{CCY}
F_{1-2} (36 and 238)	6.15E-05	-1.65E-06	4.64E-05	8.04E-08	-2.79E-08	-2.88E-09
F_{2-3} (238 and 364)	6.28E-05	1.07E-06	4.72E-05	-6.94E-08	3.13E-09	-1.92E-09
F_{3-4} (364 and 490)	6.54E-05	5.54E-07	4.94E-05	-6.03E-08	-3.11E-08	-1.38E-09
F_{4-5} (490 and 616)	6.37E-05	2.56E-06	4.74E-05	-3.67E-08	-2.60E-08	-1.08E-09
F_{5-6} (616 and 742)	6.60E-05	2.48E-06	4.92E-05	-7.63E-08	1.24E-08	-8.76E-10

Table 8. Estimated local geometric values (rad, mm, or mm/m) for different sets of two force levels.

Force (N)	E_{XX1}	E_{YX2}	E_{XY2}	E_{YY1}	$E_{C(0Y)X}$	E_{Xt0}	E_{Yt0}
F_{1-2} (36 and 238)	-0.00012	2.75E-07	-7.66E-07	-9.36E-05	3.71E-06	0.004438	5.29E-05
F_{2-3} (238 and 364)	-0.00013	4.91E-07	-7.79E-07	-9.91E-05	-6.08E-07	0.004025	0.0003
F_{3-4} (364 and 490)	-0.00014	5.27E-07	-6.77E-07	-0.00011	6.41E-07	0.003821	-0.00036
F_{4-5} (490 and 616)	-0.00014	5.01E-07	-6.68E-07	-0.0001	-5.91E-06	0.003525	-0.00093
F_{5-6} (616 and 742)	-0.00015	7.19E-07	-8.15E-07	-0.00011	-5.58E-06	0.003413	-0.00155

Fig. 15 and *Fig. 16* show the estimated experimental compliance and geometric error values. In *Fig. 15* by increasing the force the majority of compliance terms increase such as C_{XXX}, C_{XYX}, C_{YYY} and C_{CCY}. The other two, C_{CXY} and C_{CYY} show no clear trends. In *Fig. 16,* as the force increases, most of the loaded geometric terms decrease such as the scale gain errors E_{XX1} and E_{YY1}, the out-of-squareness $E_{C(0Y)X}$ and the tool offsets E_{Xt0} and E_{Yt0}. Nevertheless, some increase such as the quadratic straightness E_{YX2} and E_{XY2}.
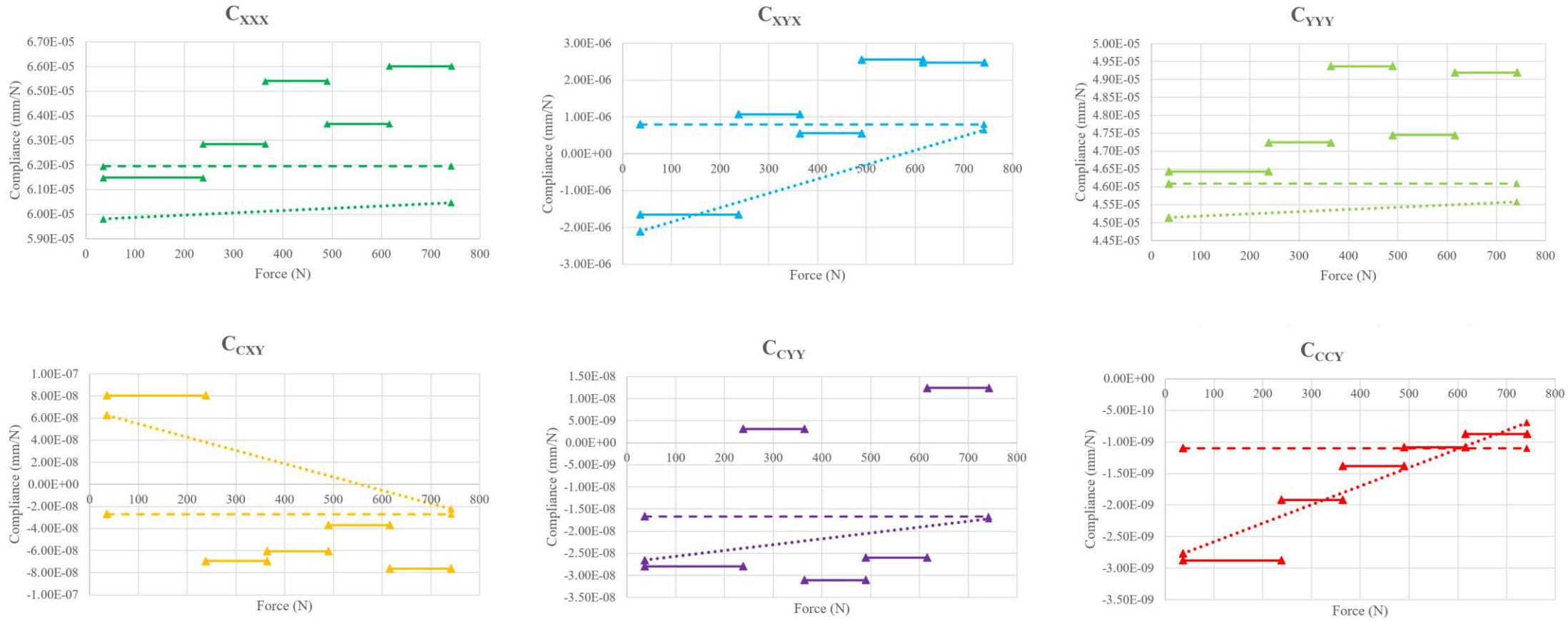
Fig. 15. Estimated local compliances were acquired employing data from two adjacent force levels (dashed and dotted lines from 36 to 742 N depict the constant and variable (linear model) global compliance value obtained by using all force results, respectively).
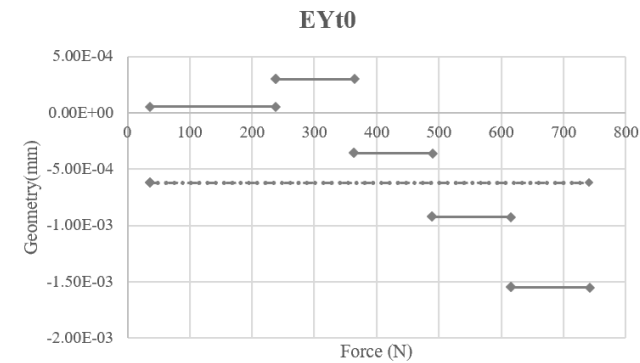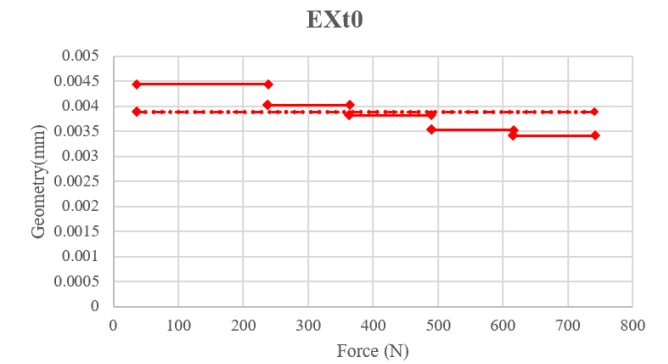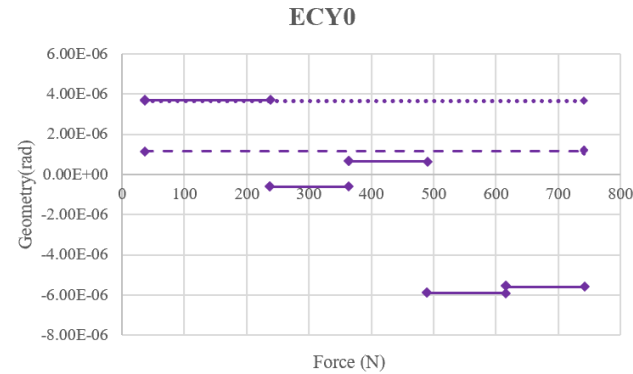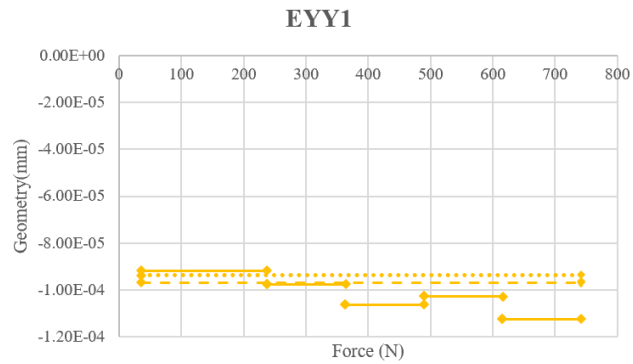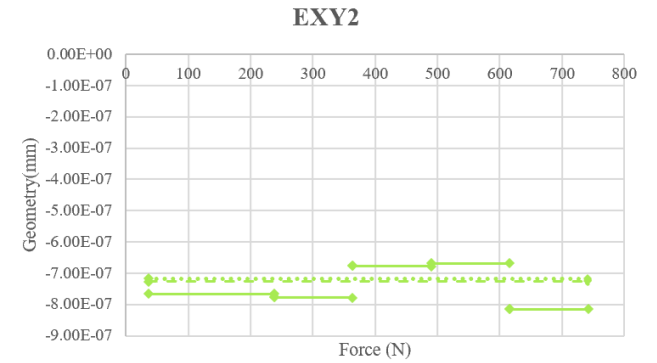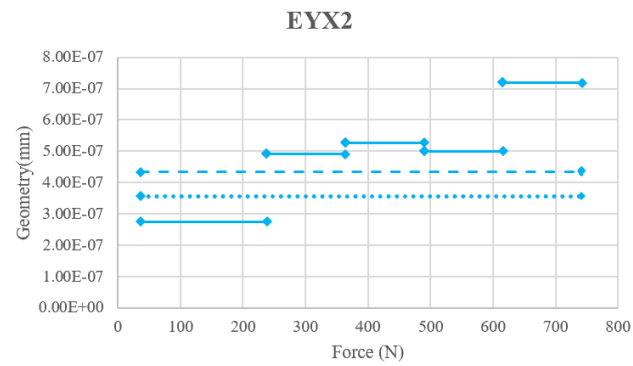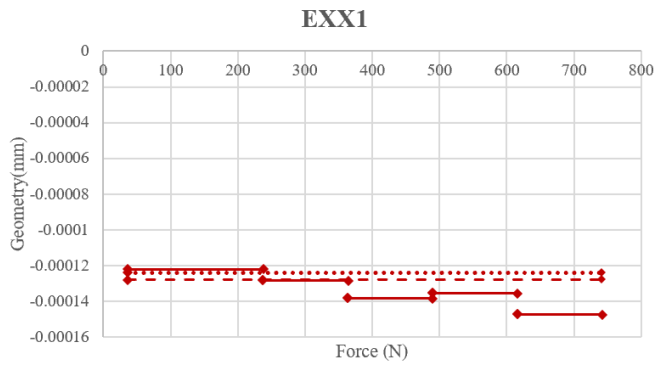
Fig. 16. Estimated local geometric parameters were acquired employing data from two continuous force levels (dashed and dotted lines from 36 to 742 N depict the constant and variable (linear model) unique global geometric parameter value for each compliance term, respectively).

5.3. Variable compliance

Results obtained for local compliances suggest that the values of compliances vary slightly with the applied load. This appears to cause changes in the estimated geometric error parameters which contravenes the definition of geometric errors that should be invariant with the applied load. To analyze the change of compliance parameters as a function of force (F) a solution is now proposed that consists of enriching the compliance model using a linear function for each compliance term such as

$$C_{XXX} = C_{XXX0} + C_{XXX1}F$$

<div align="right">Equation 33</div>

Then, the elasto-geometric Jacobian (J_{H}) in *Equation 30* is expanded to include the new linear (degree one) compliance terms by adding an adjacent column for each existing column corresponding to the constant compliance term (degree 0), which is the same value but multiplied by the relevant force level for each row. Each row corresponds to an LDBB reading at a certain location on the test circle and a certain force level. These estimated parameters as a function of force are shown in *Fig. 15* as a dotted line from 36 to 742 N. Comparing the global constant compliance and the global linearly variable compliance, it is observed that the variable compliance model better explains the change of compliance parameters, as observed in the local compliance values, as a function of force across the load range. In *Fig. 16*, both elasto-geometric models, whether using constant or linearly variable compliance terms, yield constant geometric errors as defined in the model. When comparing these constant terms with the local compliance model and the corresponding geometric errors, which change with the force level, it is observed that the global variable compliance model yields geometric error parameters that tend to be closer to the local geometric parameters at the lowest pressure values. To observe the modeling improvement of the variable compliance in comparison with constant compliance values, the root mean square error is used

<div align="right">Equation 34</div>

$$RMSE = \sqrt{\frac{\sum_{i=1}^{n}(Predicted_i - Measured_i)^2}{n}}$$

where Predicted, Measured and n represents predicted LDBB readings, experimental LDBB readings, and the number of measurements, respectively. The RMSE value for produced LDBB reading for all force levels by constant and variable compliance are 0.0011 and 0.0009 mm, respectively, which shows a further reduction of 18% using the variable compliance model. To determine how well the predicted data aligns with the measured one, the normalized root mean square error fitness is used

$$fitness\ (\%) = \left(1 - \frac{RMSE}{\left|Measured_{i,max} - Measured_{i,min}\right|}\right) \times 100 \qquad \text{Equation 35}$$

Table 9 presents the fitting percentage for predicted readings from estimated global, variable global, and local compliance parameters. The fit improves slightly with the force level as the compliance effect becomes more significant. All fitting percentages exceed 91%. Compared to the constant variable model, the linearly variable compliance model improves the fit only slightly by just over 1% when using all force level data.

Table 9. The fitting values for global, variable global, and local compliance predicted readings with different force levels.

LDBB readings for different force level	Fitting with constant global compliances	Fitting with variable (linear model) global compliance	Fitting with local compliance
ρ_{36} (%)	92.4	93.7	91.7
ρ_{238} (%)	93.0	94.2	95.3
ρ_{364} (%)	92.5	93.8	95.4
ρ_{490} (%)	93.0	94.2	95.8
ρ_{616} (%)	93.4	94.6	96.0
ρ_{742} (%)	93.9	95.0	96.2

6. Conclusion

The elasto-geometric model is contextualized to the data gathered during a loaded 2D circular test implemented using a loaded double ball bar (LDBB) to simultaneously estimate the machine tool X- and Y-axis equivalent compliances and geometric errors. The compliances are said to be "equivalent" because although only two axes are mobile during the test, the machine has five axes, and all axes may contribute to the observed volumetric deflections. At lower forces, the geometric errors are dominant whilst at higher forces compliance errors dominate. When using all data to build a single global geometry and compliance set of parameters (global constant compliance model) the radial volumetric variations due to geometric errors and compliance are estimated at 0.019 mm and 0.046 mm, respectively, making compliance dominant by more than three times. The impact of dominant and non-dominant equivalent global compliance C_{XXX}, C_{YYY}, C_{XYX}, C_{CXY}, C_{CYY} and C_{CCY} on the loaded circular test readings at the highest force level of 742 N are predicted to be around 0.045, 0.034, 0.00058, 0.0022, 0.0014, and 0.0045 mm peak-to-peak, respectively. The impact of loaded geometric parameter E_{XX1}, E_{YY1}, E_{YX2}, E_{XY2}, $E_{C(0Y)X}$, E_{Xt0} and E_{Yt0} on the loaded circular test readings are

predicted to be around 0.019, 0.014, 0.0074, 0.012, 0.00017, 0.0076 and 0.0012 mm peak-to-peak, respectively. The dominant global compliances are C_{XXX} and C_{YYY} at 0.0619 and 0.0461 µm/N, respectively.

By feeding the elasto-geometric model with pairs of adjacent force data the evolution of compliance with changes in the applied force is observed. Although theoretically unexpected, the estimated geometry changes with force levels. The radial volumetric largest change due to variation in the estimated local geometry across the range of tested forces (local model) amounts to 0.0085 mm whereas the global model radial volumetric effects due to geometric errors are estimated at 0.019 mm. This means that the estimated change in geometry is significant. As the force increases the majority of local compliance terms increase such as C_{XXX}, C_{XYX}, C_{YYY} and C_{CCY}. Two of the less significant compliances, C_{CXY} and C_{CYY}, show no clear trends. Most of the loaded geometric terms decrease such as E_{XX1}, E_{YY1}, $E_{\text{C(0Y)X}}$, E_{Xt0} and E_{Yt0} as the force increases but E_{YX2} and E_{XY2} increase. The change in local compliance suggests that the compliance varies with the applied force. As the compliance is assumed to be constant this may be causing the apparent change in the geometric error parameters at different force levels. Consequently, the compliance model was enriched as a linear function of the applied force to process all force level data at once so that the estimated geometry is kept the same at all force levels. The root mean square error (RMSE) value for predicting the radial LDBB readings using the constant and linearly variable compliance models are 0.0011 and 0.0009 mm, respectively, for an improvement of about 18% using the variable compliance model. As all models predict over 91% of the experimental radial deviations, the use of a linear compliance model results in just over 1% fitting improvement. The enriched elasto-geometric model provides a means to analyze the relative contribution of geometric errors and compliance at different load levels and could in principle be used for machine health monitoring, fault diagnosis, and compensation.

Conflict of interest

The authors declare no competing interests.

Availability of data and material

Available from the corresponding author on reasonable request.

Code availability

Available from the corresponding author on reasonable request.

Ethics approval

I declare on behalf of my co-authors that this work is original and has not been published elsewhere, nor is it currently under consideration for publication elsewhere.

Consent to participate Not applicable

Consent for publication Not applicable

References

[1]   M. A. Salgado, L. N. L. de Lacalle, A. Lamikiz, J. Munoa, and J. A. Sanchez, "Evaluation of the stiffness chain on the deflection of end-mills under cutting forces," (in English), *International Journal of Machine Tools & Manufacture,* vol. 45, no. 6, pp. 727-739, May 2005, doi: 10.1016/j.ijmachtools.2004.08.023.

[2]   A. Archenti and M. Nicolescu, "A top-down equivalent stiffness approach for prediction of deviation sources in machine tool joints," *CIRP Annals,* vol. 66, no. 1, pp. 487-490, 2017/01/01/ 2017, doi: https://doi.org/10.1016/j.cirp.2017.04.066.

[3]   X. Gao, B. Li, J. Hong, and J. Guo, "Stiffness modeling of machine tools based on machining space analysis," *The International Journal of Advanced Manufacturing Technology,* vol. 86, no. 5-8, pp. 2093-2106, 2016, doi: 10.1007/s00170-015-8336-z.

[4]   Y. Shi, X. Zhao, H. Zhang, Y. Nie, and D. Zhang, "A new top-down design method for the stiffness of precision machine tools," *The International Journal of Advanced Manufacturing Technology,* vol. 83, no. 9-12, pp. 1887-1904, 2015, doi: 10.1007/s00170-015-7705-y.

[5]   W.J. Lee and S. l. Kim, "Joint Stiffness Identification of an Ultra-Precision Machine for Machining Large-Surface Micro-Features," *International Journal of Precision Engineering and Manufacturing,* vol. 10, no. 5, pp. 115-121, 2009.

[6]   D. Kono and A. Matsubara, "Investigation on Direction Dependency of Tool-Workpiece Compliance of Machine Tool," *Procedia CIRP,* vol. 46, pp. 529-532, 2016, doi: 10.1016/j.procir.2016.03.134.

[7]   P. Pawełko, D. Jastrzębski, A. Parus, and J. Jastrzębska, "A new measurement system to determine stiffness distribution in machine tool workspace," *Archives of Civil and Mechanical Engineering,* vol. 21, no. 2, 2021, doi: 10.1007/s43452-021-00206-6.

[8]   A. Archenti and M. Nicolescu, "Accuracy analysis of machine tools using Elastically Linked Systems," *CIRP Annals,* vol. 62, no. 1, pp. 503-506, 2013/01/01/ 2013, doi: https://doi.org/10.1016/j.cirp.2013.03.100.

[9]   *ISO 230_4, Test code for machine tools — part 4: Circular tests for numerically controlled machine tools.*, International Organization for Standardization, 2005.

[10]   A. Archenti, "Prediction of machined part accuracy from machining system capability," *CIRP Annals,* vol. 63, no. 1, pp. 505-508, 2014, doi: 10.1016/j.cirp.2014.03.040.

[11]   J. B. Bryan, "A simple method for testing measuring machines and machine tools," *Precision Engineering,* vol. 4, no. 2, pp. 61-69, 1982.

[12]   Y. Kakino, Y.Ihara, Y. Nakatsu, and K. Okamura, "The Measurement of Motion Errors of NC Machine Tools and Diagnosis of their Origins by Using Telescoping Magnetic Ball Bar Method," *CIRP Annals,* 1987.

[13]   Z. Jiang, M. Huang, X. Tang, B. Song, and Y. Guo, "Elasto-geometrical calibration of six-DOF serial robots using multiple identification models," *Mechanism and Machine Theory,* vol. 157, 2021, doi: 10.1016/j.mechmachtheory.2020.104211.

[14]   S. Marie and P. Maurine, "Elasto-Geometrical Modelling of Closed-Loop Industrial Robots Used For Machining Applications," presented at the IEEE International Conference on Robotics and Automation, 2008.

[15]   S. Marie, E. Courteille, and P. Maurine, "Elasto-geometrical modeling and calibration of robot manipulators: Application to machining and forming applications," *Mechanism and Machine Theory,* vol. 69, pp. 13-43, 2013, doi: 10.1016/j.mechmachtheory.2013.05.003.

[16]   K. Kamali, A. Joubair, I. A. Bonev, and P. Bigras, "Elasto-geometrical Calibration of an Industrial Robot under Multidirectional External Loads Using aLaser Tracker," presented at the IEEE International Conference on Robotics and Automation, 2016.

[17]   K. Kamali and I. A. Bonev, "Optimal Experiment Design for Elasto-Geometrical Calibration of Industrial Robots," *IEEE/ASME Transactions on Mechatronics,* vol. 24, no. 6, pp. 2733-2744, 2019, doi: 10.1109/tmech.2019.2944428.

[18]   B. Beglarzadeh, J. R. R. Mayer, and A. Archenti, "Modelling and indirect measurement of machine tool equivalent joint compliances," *CIRP Journal of Manufacturing Science and Technology,* vol. 35, pp. 882-895, 2021, doi: 10.1016/j.cirpj.2021.10.001.

[19]   J. J. Craig, *Introduction to Robotics, Mechanics, and Control*. Pearson Prentice Hall, 2005.

[20]   G. Zhang, R. Veale, T. Charlton, B. Borchardt, and R. Hocken, "Error Compensation of Coordinate Measuring Machines," *CIRP Annals,* vol. Volume 34, no. 1, pp. 445-448, 1985.

[21]   A. ARCHENTI, T. OSTERLIND, and C. M. NICOLESCU, "EVALUATION AND REPRESENTATION OF MACHINE TOOL DEFORMATIONS," *Journal of Machine Engineering,* vol. 11, no. 4, 2011.

[22]   *ISO 3290-1, Rolling bearings- Balls- Part 1: Steel balls.*, International Organization for Standardization, 2014.

[23]   *ISO 1101, Geometrical product specifications (GPS)-Geometrical tolerancing-Tolerances of form, orientation, location, and run-out.*, International Organization for Standardization, 2017.

[24]   C. J. Evans, R. J. Hocken, and W. T. Estler, "Self-Calibration: Reversal, Redundancy, Error Separation, and 'Absolute Testing'," *CIRP Annals,* vol. 45, no. 2, pp. 617-634, 1996, doi: 10.1016/s0007-8506(07)60515-0.